



SDSS-IV MaNGA: The MaNGA Dwarf Galaxy Sample Presentation

M. Cano-Díaz¹, H. M. Hernández-Toledo², A. Rodríguez-Puebla², H. J. Ibarra-Medel³, V. Ávila-Reese²,
O. Valenzuela², A. E. Medellín-Hurtado⁴, J. A. Vázquez-Mata^{5,6}, A. Weijmans⁷, J. J. González², E. Aquino-Ortiz⁸,
L. A. Martínez-Vázquez², and Richard R. Lane⁹

¹ CONACYT Research Fellow—Instituto de Astronomía, Universidad Nacional Autónoma de México, Apartado Postal 70-264, CDMX, 04510 Mexico
mcano@astro.unam.mx

² Instituto de Astronomía, Universidad Nacional Autónoma de México, Apartado Postal 70-264, CDMX, 04510 México

³ Instituto de Astronomía y Ciencias Planetarias, Universidad de Atacama, Copayapu 485, Copiapó, Chile

⁴ Licenciatura en Ciencias de la Tierra, Facultad de Ciencias, Universidad Nacional Autónoma de México, Circuito Exterior S/N, 04510, CDMX, México

⁵ Departamento de Física, Facultad de Ciencias, Universidad Nacional Autónoma de México, Ciudad Universitaria, CDMX, 04510, México

⁶ Instituto de Astronomía sede Ensenada, Universidad Nacional Autónoma de México, Km 107, Carret. Tij.-Ens., Ensenada, 22060, BC, México

⁷ School of Physics and Astronomy, University of St Andrews, North Haugh, St Andrews KY16 9SS, UK

⁸ Instituto de Astrofísica, Pontificia Universidad Católica de Chile, Av. Vicuña Mackenna 4860, 782-0436 Macul, Santiago, Chile

⁹ Centro de Investigación en Astronomía, Universidad Bernardo O’Higgins, Avenida Viel 1497, Santiago, Chile

Received 2022 May 13; revised 2022 July 4; accepted 2022 July 27; published 2022 September 7

Abstract

We present the MaNGA Dwarf galaxy (MaNDala) Value Added Catalog (VAC), from the final release of the Sloan Digital Sky Survey-IV program. MaNDala consists of 136 randomly selected bright dwarf galaxies with $M_* < 10^{9.1} M_\odot$ and $M_g > -18.5$, making it the largest integral field spectroscopy homogeneous sample of dwarf galaxies. We release a photometric analysis of the g , r , and z broadband imaging based on the DESI Legacy Imaging Surveys, as well as a spectroscopic analysis based on the Pipe3D SDSS-IV VAC. Our release includes the surface brightness (SB), geometric parameters, and color profiles, Sérsic fits as well as stellar population properties (such as stellar ages, metallicities, and star formation histories), and emission lines’ fluxes within the FOV and the effective radii of the galaxies. We find that the majority of the MaNDala galaxies are star-forming late-type galaxies with $\langle n_{\text{Sérsic},r} \rangle \sim 1.6$ that are centrals (central/satellite dichotomy). MaNDala covers a large range of SB values (we find 11 candidate ultra-diffuse galaxies and three compact ones), filling the gap between classical dwarfs and low-mass galaxies in the Kormendy Diagram and in the size–mass/luminosity relation, which seems to flatten at $10^8 < M_*/M_\odot < 10^9$ with $\langle R_{e,r} \rangle \sim 2.7$ kpc. A large fraction of MaNDala galaxies formed from an early low-metallicity burst of SF, but also from late SF events from more metal-enriched gas: half of the MaNDala galaxies assembled 50% of their mass at $\langle z \rangle > 2$, while the last 20% was at $\langle z \rangle < 0.3$. Finally, a bending of the sSFR– M_* relation at $M_* \sim 10^9 M_\odot$ for the main-sequence galaxies seems to be supported by MaNDala.

Unified Astronomy Thesaurus concepts: Dwarf galaxies (416)

1. Introduction

Mass is a key property of galaxies that plays a fundamental role in understanding their evolution. In particular, it is notable that the distributions exhibited by the population of galaxies in several of their main properties strongly segregate by stellar mass. At $M_* \approx 2\text{--}3 \times 10^{10} M_\odot$, galaxies follow a clear bimodal distribution separated into red/passive/early-type and blue/star-forming/late-type populations, but at much larger or smaller masses, they are strongly dominated by the former or the latter, respectively. An understanding of the physics beyond this mass-dependent segregation has not yet been fully achieved (for recent reviews, see, e.g., Somerville & Davé 2015; De Lucia 2019); especially at the low-mass end, theory and observations appear to be in tension (see, e.g., Avila-Reese & Firmani 2011; Leitner 2012; Weinmann et al. 2012; Somerville & Davé 2015). Low-mass galaxies are challenging to observe, due to their low luminosity and surface brightness (SB), and thus, little is known about them as compared to their massive counterparts. The difficulty of observing them increases notably when their stellar masses are lower than

$\sim 10^9 M_\odot$, which is the typical threshold to classify dwarf galaxies (DGs) as such.

The slope of the observed galaxy luminosity function at the low-luminosity side is negative; this implies that dwarfs are the most abundant galaxies in the universe. Within the current cosmological paradigm of galaxy formation, the luminosity function, evolution, and internal properties of these galaxies depend on the nature of dark matter, but also on the effects of the baryonic processes, to which the small-scale structures are highly sensitive due to their shallow gravitational potentials. Thus, the study of DGs becomes crucial (i) to probe cosmological models and the nature of dark matter, and (ii) to understand the complex galaxy baryonic processes and evolutionary trends, such as the formation of molecular clouds and stars, including their dependence on metallicity and the UV background, as well as the feedback of stars and supernovae; for some recent reviews, see Weinberg et al. (2015), Colín et al. (2015), Bullock & Boylan-Kolchin (2017), and more references therein.

Related to item (i), estimations of the inner dynamical mass distribution of dwarfs (the “cusp-core” controversy) and the central stellar densities of massive dwarf satellites (the “too-big-to-fail” controversy) have been used as probes of dark matter type. Regarding item (ii), an important task is to infer the star formation (SF) and metallicity enrichment histories for



Original content from this work may be used under the terms of the [Creative Commons Attribution 4.0 licence](https://creativecommons.org/licenses/by/4.0/). Any further distribution of this work must maintain attribution to the author(s) and the title of the work, journal citation and DOI.

large dwarf samples, and how they depend on their mass and environment, as well as whether or not the trend of downsizing in specific SF rate (sSFR) continues below $\sim 10^9 M_\odot$. Both types of studies can greatly benefit from Integral Field Spectroscopy (IFS) observations, which allow us to obtain resolved stellar population properties and resolved kinematic information from the stellar and ionized gas components of galaxies.

Most of the previous detailed observational studies on DGs refer to the Local Group (e.g., Tolstoy et al. 2009; McConnachie 2012; Weisz et al. 2014) or to nearby clusters (e.g., Ferrarese et al. 2012; Eigenthaler et al. 2018; Venhola et al. 2019), meaning these studies are constrained to particular environments. To deeply understand and use DGs to study the small-scale challenges mentioned above, we need to explore them in much more detail in different environments, using both (resolved and unresolved) imaging and spectroscopy studies.

Early efforts at multifrequency studies of dwarfs beyond the Local Group comprised only some tens of galaxies; see, for example, Dalcanton et al. (2009; ACS Nearby Galaxy Survey Treasury Program, or ANGST), Hunter et al. (2012; Little THINGS), Ott et al. (2012; VLA-ANGST), and McGaugh et al. (2017). Geha et al. (2012) provided a valuable spectrophotometric catalog of about 3000 local field DGs ($z < 0.055$) based on the public NASA-Sloan Atlas Catalog (NSA; Blanton et al. 2011). Based on public multiwavelength data sets, Karachentsev et al. (2013) compiled a catalog of galaxies in the Local Volume (< 11 Mpc), which are mostly dwarfs. Based also on public data sets (the SDSS DR7 and other sources), Ann et al. (2015) confirmed ~ 2600 local dwarfs in the Catalog of Visually Classified Galaxies. More recently, efforts have also been made to study dwarfs beyond the Local Group using resolved stellar maps (e.g., Crnojević et al. 2016, for dwarfs around the elliptical galaxy NGC 5128). Also, using deep imaging information from multiwavelength surveys, studies of dwarf satellites around Milky Way analogs (Bennet et al. 2017; Mao et al. 2021; Carlsten et al. 2021), dwarfs in the field (Tanoglidis et al. 2021), and dwarf pairs/groups (TiNy Titans; TNT survey; Stierwalt et al. 2015, 2017) were carried out. Based on a recent deep imaging survey aimed to study low surface brightness (SB) features (including DGs) in the outskirts of nearby massive early-type galaxies (the Mass Assembly of early Type gaLaxies with their fine Structures; MATLAS), Habas et al. (2020), presented the sample selection and photometric properties of 2210 candidate dwarfs, while in Poulain et al. (2021), the structure and morphology of these galaxies were determined.

Using IFS observations and applying the spectral inversion method, based on fits of a composition of single stellar populations (SSPs) models to the spectra, inferences about the global and spatially resolved archeological properties of the galaxies and their evolution can be made (for a recent review, see Sánchez 2020). Specifically, global and radial stellar masses and SF histories of galaxies can be derived (e.g., Pérez et al. 2013; Ho et al. 2016; Ibarra-Medel et al. 2016; Sánchez et al. 2019; Neumann et al. 2020), as well as studies about the SF and the processes that quenched them (e.g., Catalán-Torrecilla et al. 2017; Schaefer et al. 2019; Cano-Díaz et al. 2019; Lacerna et al. 2020). IFS data also allow us to study the nature and effects of the AGNs in galaxies (e.g., Mingozzi et al. 2019; Sánchez et al. 2018; Wylezalek et al. 2018), as well as

their spatially resolved kinematics (e.g., Raouf et al. 2021; Garma-Oehmichen et al. 2020; Aquino-Ortíz et al. 2020).

In recent years, the first very large IFS galaxy surveys have been completed. The largest is the Mapping Nearby Galaxies at APO (MaNGA; Bundy et al. 2015), which has observed $\sim 10,000$ local galaxies ($z < 0.15$) across 1.5 or 2.5 effective radii R_e . Although MaNGA has been designed to roughly uniformly cover the stellar mass range of $10^9 < M_*/M_\odot < 10^{12}$, a small fraction of galaxies were observed at smaller masses, including those from an ancillary program dedicated to observe dwarfs (P.I. M. Cano-Díaz). The goal of this paper, which is the first in a series, is to present the sample of MaNGA galaxies with masses $M_* \lesssim 10^9 M_\odot$, which are mostly bright dwarfs (all retrieved from the final data release, DR17; Abdurro'uf et al. 2021). To our knowledge, with 136 galaxies, this is the first large sample of DGs with IFS observations

We present here the selection criteria and basic photometric and spectroscopic characterizations of this sample, named the MaNGA Dwarf Galaxy (MaNDala), using the MaNGA IFS data and multiband photometric optical images coming from the DESI Legacy Imaging Surveys (Dey et al. 2019). Using the IFS data, with the Pipe3D code and its recent improvement, pyPipe3D (Sánchez et al. 2016a, 2018, Sánchez, et al. submitted), we perform spectral and archeological analyses to characterize the level of star-forming activity of the MaNDala galaxies and determine their global mean ages and stellar metallicities (mass- and luminosity-weighted). From the photometric analysis, we obtain one-dimensional radial SB and color profiles, as well as geometric parameters. This analysis contains a wealth of useful information that allows us to review the global structural properties of the MaNDala sample, but also allows us to infer useful diagnostics for the presence of relevant inner structures as well as for more subtle structures like warps at the outer regions.

The extensive set of results for the MaNDala dwarfs coming from the two complementary data samples mentioned above will be useful for a diversity of studies, in which we intend to explore different aspects of the nature of these galaxies. All of our results will be publicly available in the form of a Sloan Digital Sky Survey IV (SDSS-IV) Value Added Catalog (VAC).¹⁰

The structure of the paper is as follows. In Section 2, we describe the photometric and spectroscopic data used for this work. In Section 3, the sample selection is described. The photometric and spectroscopic analyses are described in Section 4, while their results are reported in Section 5. Finally, in Section 6, we give our summary and discussion.

Throughout this paper, we assume a Chabrier (2003) initial mass function (IMF) and the following cosmology: $H_0 = 70 \text{ km s}^{-1} \text{ Mpc}^{-1}$, $\Omega_M = 0.3$, and $\Omega_\Lambda = 0.7$.

2. Data

2.1. DESI Images

The DESI Legacy Imaging Surveys (Dey et al. 2019) are a combination of three imaging surveys that have mapped contiguous areas of the sky in three optical bands (g , r , and z) to depths ~ 2 mag deeper than the Sloan Digital Sky Survey imaging (SDSS; e.g., Abazajian et al. 2009). The three surveys are (i) the DECam Legacy Survey (DECaLS) using the Blanco

¹⁰ Please refer to the [Appendix](#) for further information.

4 m telescope and the Dark Energy Camera (DECam; Flaugher et al. 2015), (ii) the Mayall z -band Legacy Survey (MzLS) using the Mosaic3 camera (Dey et al. 2019) at the Mayall Telescope, and (iii) the Beijing–Arizona Sky Survey (BASS) using the Bok 2.3 m telescope/90Prime camera at Kitt Peak (Williams et al. 2004). The primary goal of the Legacy Surveys is to provide targets for the Dark Energy Spectroscopic Instrument (DESI; DESI Collaboration et al. 2016).

The present work is based on the ninth release of the Legacy Surveys project (LS DR9), which contains data from all of the individual components of the Legacy Surveys (BASS, DECaLS, and MzLS). It was built on DR8 by improving the reduction techniques and procedures used for the Legacy Surveys. The images of the MaNDala DGs were retrieved in the grz bands, specifying pixel scale (0.262 arcsec/pix) and size (800×800 pixels), centered on the r.a. and decl. positions appropriate for our image postprocessing.

We adopt the flux calibration for BASS, MzLS, and DECaLS on the AB natural system of each instrument, respectively. Since the brightnesses of objects are all stored as linear fluxes in units of nanomaggies, we adopted the conversion from linear fluxes to magnitudes as described in the Photometry section of the Data Release Description.¹¹ Notice that the fluxes can be negative for faint objects, and that this was the case for some of our faintest objects. As representative values, we take median 5σ point-source (AB) depths for areas with different numbers of observations in the different regions of DR9 as $g = 24.7$ mag $r = 24.0$ mag and $z = 23.0$ mag¹²

2.2. MaNGA Spectroscopic Data

MaNGA (Bundy et al. 2015) is one of the main projects of the SDSS-IV international collaboration (Blanton et al. 2017). This project had used the IFS technique to observe over 10,000 galaxies by the end of its operations in 2020. Data were acquired with a dedicated 2.5 m telescope at the Apache Point Observatory (APO; Gunn et al. 2006). To observe the main targets, this project used Integral Field Units (IFUs) with different fiber bundles, ranging from 19 to 127 fibers, where each fiber has a diameter of $2''$ (Drory et al. 2015). This observational setup has a spectral coverage ranging from 3600 to 10,300 Å at a resolution of $R \sim 2000$ provided by the dual-beam BOSS spectrographs (Smee et al. 2013). Smaller fiber bundles were used in simultaneous observations along with the main targets, to perform sky subtraction and flux calibrations (Yan et al. 2016). A three-point dithering strategy was used for all the observations in order to achieve a complete spatial coverage of the sources within the defined apertures (for these and further details about the observing strategy, please refer to Law et al. 2015). We used the 3.1.1 version of the MaNGA reduction pipeline (Law et al. 2016), which delivers sky-subtracted, wavelength- and flux-calibrated data cubes as final data products.

3. Sample Selection

The MaNGA sample (Wake et al. 2017) consist of galaxies of all morphological types, redshifts in the range $0.01 < z < 0.15$, and stellar masses, M_* , between 10^9 and $10^{12} M_\odot$. Even though the MaNGA Survey has limits in M_* ,

there is a small fraction of galaxies outside them in the final sample. The MaNDala Sample contains galaxies that surpassed the MaNGA lower limit in M_* , but also galaxies that are part of an ancillary program to specifically observe DGs with the MaNGA observational setup.¹³

To define our sample, we selected all the galaxies within the final MaNGA sample that have $M_* < 10^{9.06} M_\odot$,¹⁴ after which we obtained 152 galaxies. The stellar masses were retrieved from the NASA-Sloan Atlas Catalog (NSA Catalog¹⁵; Blanton et al. 2011), where the Chabrier (2003) initial mass function has been used. We used the available masses derived from a Sérsic fit, and corrected their values to be in units of $h^{-2} M_\odot$, considering a value of $h = 0.70$, instead of $h = 1$ as reported in that catalog. Then we discarded all galaxies that are brighter than the Large Magellanic Cloud, following a criterion similar to the one described in Blanton & Moustakas (2009). We eliminated all galaxies that have an absolute magnitude in the g SDSS photometric band reported in the NSA Catalog < -18.5 . After this cut, we end up with 142 galaxies. We finally discarded the objects for which we did not find a complete set of MaNGA data products, whose imaging data was not optimal, or that were suspected to be stars. This final cleanse of the sample reduced it to a final sample of 136 galaxies.

These 136 galaxies comprise the first version of the SDSS-IV VAC named MaNDala (V1.0), which is part of the seventeenth data release (DR17) of the SDSS collaboration, the details of which are reported in the Appendix.

In Figure 1, we show the luminosity distance, D_L , and M_* distributions in the upper and lower panels, respectively, for this first version of the MaNDala sample. In the lower panel, we also show the relation between redshift and M_* for our sample. We find that the MaNDala sample has the following limits in distance: $0.89 < D_L/\text{Mpc} < 143.37$, with a mean of 77.48 Mpc. In the case of M_* , its range is $7.53 < \log(M_*/M_\odot) < 9.06$, with a mean of $\text{Log}(M_*/M_\odot) = 8.89$. This makes it evident that our sample is biased toward galaxies that have M_* near the limit we imposed for the selection. The above suggests that our sample consists mainly of bright DGs; however, we leave the details about the sample characteristics to be presented in the Results Section (Section 5.3.3).

4. Photometric and Spectroscopic Analysis

In this section, we describe the photometric analysis of the MaNDala galaxy sample based on the DESI images (Section 4.1), as well as our Sérsic fits (Section 4.2). In Section 4.3, we describe the spectral analysis performed to the MaNGA data.

4.1. Isophotal Analysis

We follow the iterative method of Jedrzejewski (1987) to fit the isophotes of galaxies in the g -, r -, and z -band images from the DESI Legacy Imaging Surveys with a set of ellipses using the IRAF¹⁶ task ELLIPSE. In our implementation, the ellipses are sampled along the semimajor axis of a galaxy in

¹³ <https://www.sdss.org/dr17/manga/manga-target-selection/ancillary-targets/dwarf-galaxies-with-manga/>

¹⁴ Galaxies were originally selected with $M_* < 10^{8.75} h^{-2} M_\odot$.

¹⁵ <http://www.nsatlas.org>

¹⁶ (Image Reduction and Analysis Facility) is distributed by the National Optical Astronomy Observatory, which is operated by the Association of Universities for Research in Astronomy, Inc., under cooperative agreement with the National Science Foundation.

¹¹ <https://www.legacysurvey.org/dr9/description/>

¹² <https://www.legacysurvey.org/>

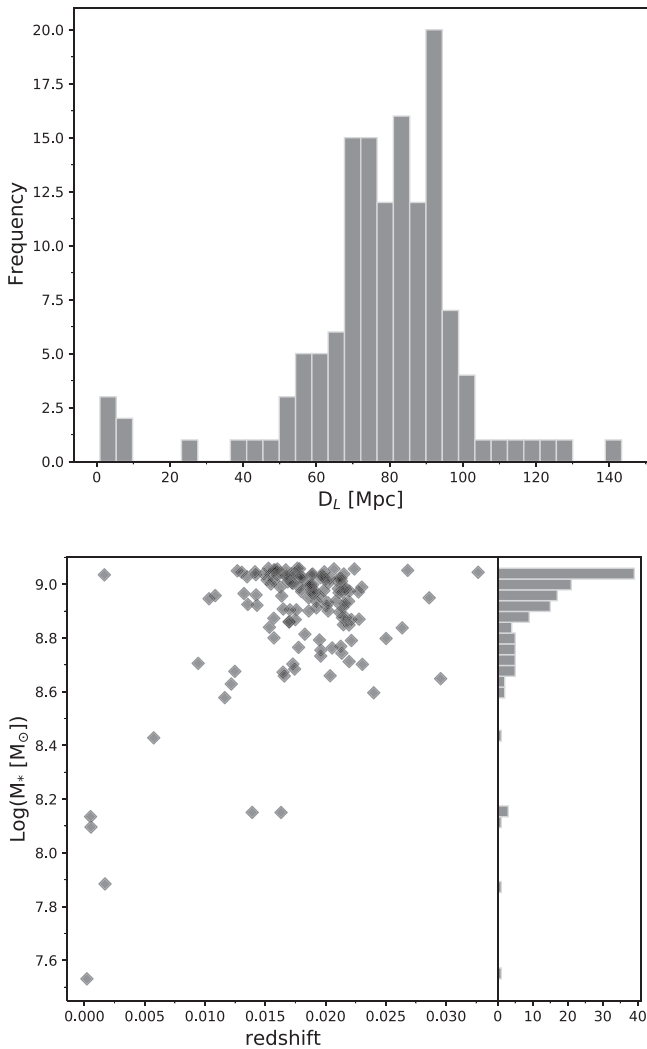


Figure 1. Upper panel: histogram representing the luminosity distance distribution of the 136 galaxies that comprise the current version of the MaNDala sample. Lower panel: relation between the redshift and M_* for the galaxies in our sample, along with the distribution of M_* . Redshifts and M_* are retrieved from the NSA Catalog.

logarithmic intervals, most of the time starting from the intermediate to outer regions and decreasing the radius of each successive ellipse by a factor of ~ 0.9 . A trial-and-error procedure was used with different starting major-axis lengths to check the stability of the extracted parameters.

To estimate the center of a galaxy, we proceed as follows. For regular-shaped galaxies, we used the barycentric position of the light distribution in the central $5 \text{ pix} \times 5 \text{ pix}$ region in the r -band images after applying IRAF image routines. For irregular-shaped galaxies with strong clumps and dusty regions, a careful masking of those clumpy regions was carried out and the center was estimated by applying the best-fit ellipses starting from the outermost regions toward the central region, setting the center, position angle (PA), and ellipticity (ϵ) as free parameters.

The r -band images were selected as the fiducial reference because of their relative lower sensitivity to dust extinction, high signal, and relatively good seeing. Once the center was estimated, it was fixed and the fitting started from the intermediate/outer regions of a galaxy while the position angle (PA) and ellipticity (ϵ) were set as free parameters. Different

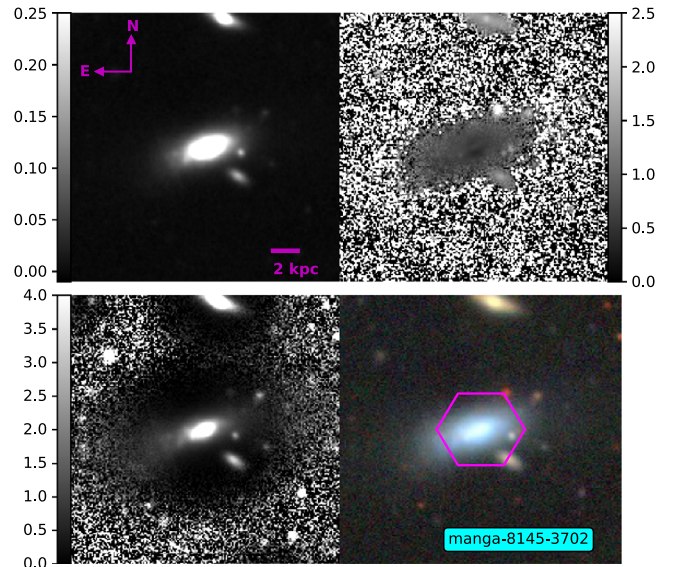


Figure 2. Mosaic displaying the images derived from the photometric analysis for the galaxy MaNGA-8145-3702. Upper panels: r -band DESI image (left) and $g - z$ 2D color map (right). Lower panels: g -band DESI image with a Gaussian filter (left) and RGB DESI image. The hexagon in the RGB image represents the MaNGA field of view.

values of the initial outer semimajor axis length were tried, allowing us to check the consistency of the fitted ellipses and their quality flagging.

A final step considers the extraction of the average isophotes in the g and z bands by using as a reference the already estimated r -band isophotal parameters. The above is intended to ensure the extraction of a uniform profile and allow for an estimate of color profiles from the combination of different bands.

As stated in the DESI DR9 description,¹⁷ the pipeline removes a sky level that includes a sky pattern, an illumination correction, and a single, scaled fringe pattern. These corrections are intended to make the sky level in the processed images nearly zero, and to remove most pattern artifacts. In practically all cases in the MaNDala sample, the galaxy image is small enough that our retrieved frames contain portions of the sky unaffected by the galaxy, so the sky background corrections already implemented are adopted without any further correction.

We also derived various image products from the reduced, calibrated images, namely, color index ($g - z$) maps and filter-enhanced images in the r -band optimized to enhance inner structures as well as low-SB outer structures. These images were combined with the available RGB color images from the DESI legacy archives to generate image mosaics for each galaxy; these mosaics are very useful for the visual recognition of morphological details.

In Figure 2, we show an example of the product images for the galaxy MaNGA-8145-3702, in the form of a mosaic. In the clockwise direction and from the top left: an r -band DESI image, a $g - z$ 2D color map, an RGB DESI image, and a g -band DESI image postprocessed with a Gaussian kernel ($\sigma = 15$) and normalized to enhance low-SB features over the background.

¹⁷ www.legacysurvey.org/dr9/description/

4.2. Geometric Parameters and Surface Brightness Profiles

The ELLIPSE task in the IRAF STSDAS package estimates the intensity distribution along ellipses, which are expressed as a Fourier series:

$$I(\phi) = I_o + \sum a_n \sin(n\phi) + \sum b_n \cos(n\phi), \quad (1)$$

where ϕ is the ellipse eccentric anomaly, I_o is the mean intensity along the ellipse, and a_n and b_n are harmonic amplitudes.

The fitting started in the intermediate regions of galaxies, going first to the outer regions, up to a point where the mean counts are comparable to the σ sky background. At this point, the algorithm then goes back to the central regions and stops at the specified first central pixel.

Foreground stars as well as apparently nearby galaxies and other image artifacts like diffracting patterns were carefully masked before ellipse fitting. However, in some galaxies, the fitting could be distorted by mergers or the contaminating light from advanced galaxy interactions that our masking could not eliminate, causing ϵ and PA to deviate to an arbitrary trend. In these cases, we proceeded with the ellipse fitting either stopping near the edge of the galaxy or stopping farther out but taking note of these circumstances.

Ellipse fittings proceeded by keeping the center fixed and allowing the ϵ and PA parameters to vary in order to maximize the detection of inner structures like bars and other prominent features. Notice, however, that the fitting may be affected in the very central regions, due to algorithm indeterminacy in the innermost 3–4 pixels, as described in the documentation of the ELLIPSE task in IRAF (see also Jędrzejewski 1987), or by seeing effects.

We propagate the errors on I into errors on μ in magnitude units. The surface brightness profiles in the g and z bands are constrained to have the same geometric parameters as determined in the r band. To build 1D color profiles, we proceeded by subtracting point-to-point the surface brightness of the g band from that of the z band, from the central regions up to where the SB profile of the z band attains a 1σ SB limit, typically at ~ 27.7 mag arcsec $^{-2}$ according to our own estimates, based on the corresponding variance images.

Finally, all SB profiles were inspected in order to ensure positive values. In cases of negative values at the end of their SB profiles, those points were excluded. The presence of negative values was more frequently found in the z band, suggesting the influence of the background level at brighter levels compared to those in the g and r bands. A final cut of all the SB profiles is based on our own depth limits estimates for each galaxy in the three DESI photometric bands.

The three surveys (DECaLS, BASS, and MzLS) use a three-pass strategy to tile the sky. This strategy is designed to account for the gaps between CCDs in the cameras, to ensure that the surveys reach the required depth, to remove particle events and other systematics, and to ensure photometric and image quality uniformity across the entire survey. For the Legacy Surveys, a postprocessing catalog generation pipeline called legacypipe was created and The Legacy Surveys footprint was analyzed.¹⁸

Among the different images there contained, the label “imag” refers to files with the image pixels, the label “invva” refers to the surface brightness uncertainties (inverse-variance)

images, while the labels “psfdepth” and “galdepth” refer to estimates of the point-source or compact-galaxy detection levels. To estimate SB limits on an individual basis, we have retrieved the “invvar” images containing $1/\sigma^2$ for the pixels in the grz bands and proceeded by reproducing our isophotal analysis (adopting the geometric ϵ , PA , and R_{\max} already obtained for the “image” files) on those images. Our (5σ) SB limits correspond to an isophotal annulus region around R_{\max} in each band. For 119 galaxies, their positions were close to the center of the retrieved inverse-variance maps. For the remaining galaxies, their positions appeared off-centered, so we proceeded with the SB limit estimates only after a more careful identification of each galaxy on these maps. The mean values of these limits are 27.69, 27.02 and 25.92 mag arcsec $^{-2}$ for the g , r , and z bands, respectively. The individual SB limits for each galaxy in the grz bands are retrievable directly from our website.¹⁹ These limits are the ones adopted when performing Sérsic fits to the SB profiles and other analyses described in the forthcoming sections.

In Figure 3, we show an example of the collection of profiles that emerge from the photometric analysis for the galaxy MaNGA-8145-3702, which has already been presented in Figure 2. In the clockwise direction, starting from the top left panel, we show the following profiles: ellipticity (ϵ) measured in the r band, SB profiles for the z , r , and g bands (in yellow, red, and black respectively), the cumulative flux in the r band, the Sérsic fits to the SB profiles (to be explained in Section 4.2.1), the $g-z$ and $g-r$ color profiles (in blue and magenta respectively), and the P.A. measured in the r band.

4.2.1. Sérsic Fit

Here, we describe the fitting process to the SB profiles of the MaNDala galaxies.

As it is often in the literature, we assume that the SB profiles of the galaxies are well-described by a Sérsic (1963) function:

$$I(R) = I_e \exp\left(-b_n \left[\left(\frac{R}{R_e}\right)^{1/n} - 1\right]\right), \quad (2)$$

where R_e is effective radius, n is the Sérsic index, I_e is the amplitude of the SB at R_e , and b_n is such that $\gamma(2n, b_n) = \Gamma(2n)/2$ (where Γ and γ are respectively the complete and incomplete gamma functions). In this paper, we use the analytical approximation for b_n reported in Ciotti & Bertin (1999), which we assume to be valid for $0.5 \leq n \leq 10$. We note that, in this paper, the variable R refers to the radius along the semimajor axis of the SB profiles. Therefore, the effective radius, R_e , reported here will refer to the effective radius along the semimajor axis.

The effects of seeing on the SB profiles of MaNDala galaxies are introduced by assuming that the PSF from the DESI images are well-described by a Moffat (1969) function with $\beta = 2.480, 2.229$, and 1.999 for the g , r , and z bands, respectively, (DESI help desk and Imaging Survey Experts, private communication). Thus, here we convolve the Sérsic profile, Equation (2), by a Moffat PSF (for a discussion, see Trujillo et al. 2001); we will denote the above by I_{conv} . That is, assuming that the 1D profile is in elliptical coordinates $(x, y) = (\xi \cos \theta, \xi(1 - \epsilon) \sin \theta)$, then the convolved SB along

¹⁸ For the index of the Legacy Survey products, see <https://portal.nersc.gov/project/cosmo/data/legacysurvey/dr9/>.

¹⁹ <https://mandalasample.wordpress.com/download/>

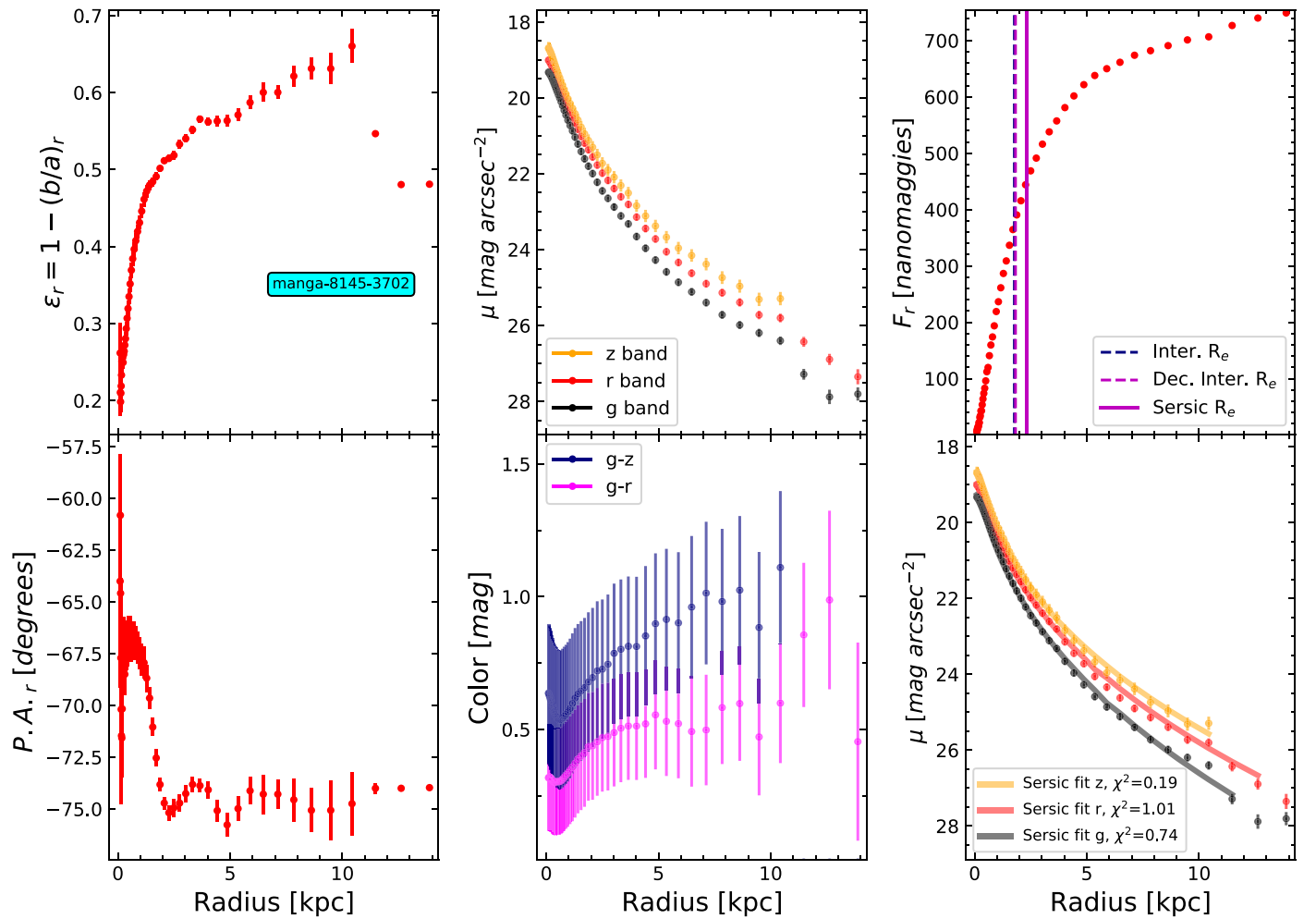


Figure 3. Example of the radial profiles derived from the photometric analysis for the MaNGA-8145-3702 galaxy. Top panel, from left to right: ellipticity (ϵ) measured in the r band, surface brightness profiles for the z , r , and g bands (in yellow, red, and black, respectively) and the cumulative flux in the r band, along with three estimates of the R_e , from an interpolation of this curve, from the same interpolation but deconvolving with the PSF, and from the Sérsic fit in the r band. Bottom panels, from left to right: P.A. measured in the r band, the $g - z$ and $g - r$ color profiles (in blue and magenta, respectively), and Sérsic fits to the surface brightness profiles for the three bands, displayed in the same color code as the top middle panel.

the semimajor axis, $\theta = 0$, is given by

$$I_{\text{conv}}(\xi) = (1 - \epsilon) \int \int \text{PSF}(\xi', \theta', \xi) I(\xi') \xi' d\xi' d\theta'. \quad (3)$$

Here, ϵ is the ellipticity, which for simplicity we assume to be constant and equal to its average value for each galaxy.

The methodology to determine the best-fit parameters of Equation (2) for every galaxy in the MaNDala sample is as follows:

1. As an initial guess, we use the R_e from the photometric analysis described in a previous subsection and compute $\mu_e (= -2.5 \log I_e)$ from the observed SB profiles. Initially, we assume that all galaxies have a Sérsic index of $n = 2.5$.²⁰
2. We sample the best-fit parameters that minimize the likelihood function $L \propto e^{\chi^2/2}$ by using the Markov Chain Monte Carlo method (described in Rodríguez-Puebla et al. 2013) and the initial values described in the previous item. We run 10 chains consisting of 10^4

elements each, and χ^2 is given by

$$\chi^2 = \sum_{i=1}^{N_{\text{bin}}} \left(\frac{\mu_{i,\text{model}} - \mu_{i,\text{obs}}}{\sigma_{i,\text{obs}}} \right)^2, \quad (4)$$

where N_{bin} is the number of radial bins in the observed SB profiles $\mu_{i,\text{obs}}$ of each galaxy and $\sigma_{i,\text{obs}}$ is its corresponding error, and $\mu_{i,\text{model}}$ represents the SB profiles given by Equation (2). As a result, we find the best-fit parameters to μ_e , n , and R_e that minimize Equation (2).

3. Next, we use the best-fitting parameters and the covariance matrix constrained above as the initial guess for finding the best-fit parameters of the convolved Sérsic profile, $I_{\text{conv}}(R)$. We do so by replacing in Equation (4) μ_{model} by $\mu_{\text{conv-model}}$. Here, we sample three chains consisting of 500 elements each.²¹

The best-fitting parameters described here are fitted to each band independently. That is, we do not make any assumption on the wavelength dependence of the Sérsic profile parameters.

²⁰ This is a reasonable assumption because $n = 2.5$ is halfway between disks and spheroids.

²¹ The number of elements and chains is reduced because this is a computationally intensive calculation. However, we find that the above setting is sufficient to sample the space parameter, due to the optimization in the priors.

The bottom right panel of Figure 3 shows an example of the best-fit Sérsic profiles for the observed SB profiles of MaNGA-8145-3702 galaxy. The inset in the same panel shows the reduced χ^2 defined as $\chi^2/(\text{d. o. f.})$, where $\text{d. o. f.} = N_{\text{bin}} - 3$.

4.3. Spectroscopy Analysis

For this work, we use the data products provided by the 3.1.1 version of the SDSS-IV Pipe3D Value Added Catalog²² (VAC; Sanchez et. al submitted, Sánchez et al. 2018). For our purposes, we have homogenized these data products to be consistent with the cosmological model adopted by us (Pipe3D VAC data products use: $H_0 = 71$ km/s/Mpc, $\Omega_M = 0.27$, $\Omega_\Lambda = 0.73$).

Here, we briefly summarize how PYFIT3D works (for more details, we refer the reader to Sánchez et al. 2016a, 2016b; Lacerda et al. 2022): A spatial binning is first performed in order to reach an S/N of 50 per bin across the entire field of view (FoV). A nonparametric stellar population synthesis (SPS) analysis is then applied to the co-added spectra within each spatial bin. The SPS analysis fits the continuum to a composed set of simple stellar populations (SSPs) of 39 ages, linearly spaced for ages of <0.02 Gyr and logarithmically spaced at larger ages, and seven metallicities: $Z_\star = 0001, 0005, 0.0080, 0.0170, 0020, 0.0300, \text{ and } 0.0400$. The SSPs were generated with an updated version of the BRUZUAL & CHARLOT 03 SPS models (Bruzual et al. in prep., Sanchez et al., submitted), using the MaSTAR stellar library (Yan et al. 2019) and a Salpeter (1955) IMF. We refer to this set as `sLOG`. The use of `sLOG` improves the SPS for the MaNDala galaxies mainly by extending the metallicity range to lower values. Finally, the Cardelli et al. (1989) extinction law is used in the calculation of the dust attenuation.

PYPIPE3D rescales the stellar population models for each spaxel within each spatial bin to the continuum flux intensity in the corresponding spaxel, and generates a set of spatially resolved maps of the SPS properties. In this paper, we used the information from the spatially resolved maps of the luminosity- and mass-weighted stellar ages in each spaxel that are calculated as logarithmic averages:

$$\log(\text{age}_{mw}) = \sum_j^{n_{ssp}} \log(\text{age}_{ssp,j}) m_{ssp,j} / \sum_j^{n_{ssp}} m_{ssp,j}, \quad (5)$$

$$\log(\text{age}_{lw}) = \sum_j^{n_{ssp}} \log(\text{age}_{ssp,j}) L_{ssp,j} / \sum_j^{n_{ssp}} L_{ssp,j}, \quad (6)$$

where the j SSP is characterized by the age $\text{age}_{ssp,j}$, luminosity $L_{ssp,j}$, and mass $m_{ssp,j}$; n_{ssp} is the total number of SSPs. The mass- and luminosity-weighted stellar metallicities are calculated in the same way. We use the mass- and luminosity-weighted age and metallicity maps to derive the respective stellar ages and metallicities up to R_e and the entire FoV, in the r band. To estimate the aperture within R_e , we use the $P.A.$ and ellipticity values reported in this work, while the FoV aperture corresponds to the IFU bundle area of the given target.

4.3.1. Ionized Gas Emission Lines

PYPIPE3D subtracts the fitted stellar population models from the original data cube to create a cube comprising only the ionized gas emission lines (and the noise). Individual nebular emission line fluxes are then calculated segment-by-segment using a weighted momentum analysis based on the kinematics of $\text{H}\alpha$ (Sánchez et al. 2022; Lacerda et al. 2022). From the obtained emission line maps, we integrate the ionized gas line fluxes within the two apertures mentioned above, R_e and the FoV of each galaxy. To avoid contamination of any nearby star within our apertures, we used a set of star masks derived from the GAIA star positions. These star masks are described in Sánchez et al. (2022). The nebular emission lines used in this work are: $\text{H}\beta$, $\text{H}\alpha$, $[\text{O III}]\lambda 5007$, $[\text{N II}]\lambda 6584$, $[\text{S II}]\lambda 6716$, $[\text{S II}]\lambda 6731$, and $[\text{O I}]\lambda 6300$. We estimate the total equivalent widths (EW) of $\text{H}\alpha$ within a given aperture by dividing the total emission line flux by the integrated stellar continuum within the same aperture.

5. Results

5.1. Basic Morphological Classification

The MaNGA Visual Morphology Catalog²³ (Vázquez-Mata et al. 2022) provides a classification in terms of the Hubble Sequence for MaNGA galaxies. Since the MaNDala sample is a subset of the complete MaNGA sample, that classification has been inherited here. Although other classification schemes are more appropriate for dwarf galaxies (see, for example, Kim et al. 2014), such classification is not available at this time for the MaNDala sample, ergo we preferred to keep the Hubble classification only for descriptive purposes. In line with this, we describe the classification in terms of two broad types of Hubble groups: early types, comprising E and Sa types, and late types, comprising types equal to or later than Sab.

We are aware that the classification scheme chosen is tentative and that a more detailed classification, using the specific morphological types for dwarfs, is required. However, for the purpose of this work, it is sufficient to have this basic morphological information. We were able to provide a classification for 135 galaxies from our sample, with one remaining, due to its intrinsic faintness. Our results show that 25 belong to the early group ($\sim 19\%$) and 110 to the late ($\sim 81\%$). As expected, the vast majority of the galaxies in our sample of bright dwarfs fall within the late morphological group, which contains mostly very late to irregular types.

5.2. Environment

A simple way to characterize the environment of galaxies is dividing them between central and satellites. For this purpose, we make use of the information given in the SDSS-IV Galaxy Environment for MaNGA VAC (GEMA),²⁴ which utilizes the methodology described in Yang et al. (2007) to identify galaxy groups composed of a central galaxy and its satellites. In this catalog, there are 121 MaNDala galaxies, for which we identify 86 centrals and 35 satellites. Eighty-two of the central galaxies are the most massive within their respective groups, and 76 of them belong to a group of only one galaxy. Another way to characterize the environment of a DG is via the distance to its

²² <https://www.sdss.org/dr17/manga/manga-data/manga-pipe3d-value-added-catalog/>

²³ https://www.sdss.org/dr17/data_access/value-added-catalogs/

²⁴ https://www.sdss.org/dr17/data_access/value-added-catalogs/?vac_id=gema-vac-galaxy-environment-for-manga-value-added-catalog

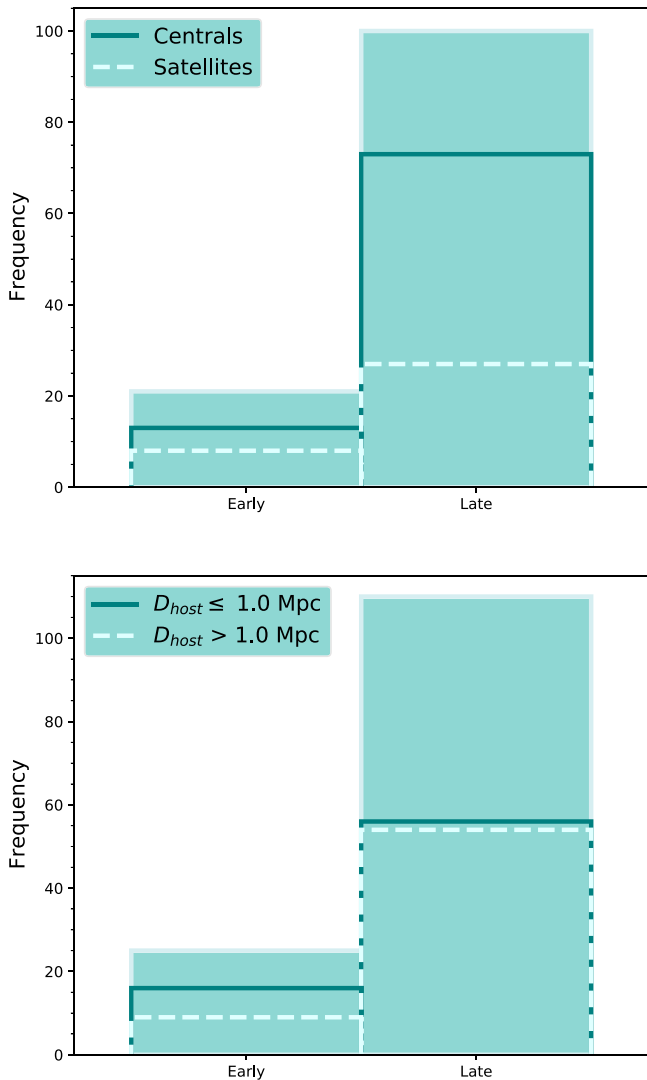


Figure 4. Upper panel: filled green bars show the histogram of the two morphological types for the 121 MaNDala galaxies with central/satellite information available in the GEMA Catalog. Empty bars show the histograms for the same morphological types, but only for central and satellite galaxies, in solid and dashed lines, respectively. Lower panel: filled green bars show the histogram of the two morphological types for the 135 MaNDala galaxies with information from Geha et al. (2012) on the distance, D_{host} , to the nearest luminous galaxy. Solid and dashed line bars show the histograms for field ($D_{host} > 1$ Mpc, relatively isolated) galaxies and those in more dense environments ($D_{host} \leq 1$ Mpc).

nearest luminous neighbor, D_{host} . To achieve this, we use the determinations of this parameter given in Geha et al. (2012). Their environment criterion is defined in the following way: a galaxy beyond $D_{host} > 1.5$ Mpc (within 1000 km s^{-1} in redshift) of a luminous host galaxy is defined to be in the field, which implies that it is relatively isolated; otherwise, it is considered not to be isolated. We have this information for all of the galaxies in our sample; however, we relax the environment criterion while using a threshold value of 1 Mpc for D_{host} , for which we identify 63 ($\sim 46\%$) to be in the field and 73 ($\sim 54\%$) in denser environments. The main reason for changing the value of D_{host} is because clusters of halo mass $M_{vir} \sim 10^{14} M_{\odot}$ are larger than ~ 1 Mpc. This means that the value adopted by Geha et al. (2012) could be larger than the cluster environment; in other words, their field galaxies would be biased to very low density environments.

In the upper panel of Figure 4, we present a histogram of the morphological types for the 121 galaxies in our sample found in the GEMA Catalog. The filled green bars represent the complete set of 121, galaxies separated into early and late types. The solid line bars correspond to those galaxies identified as centrals, while the dashed line bars correspond to the satellites. In the lower panel, we show a similar histogram, in which the filled bars represent the 135 galaxies for which we have morphological and environmental information from Geha et al. (2012), with dashed and solid line bars corresponding to field and denser environments, respectively. Central dwarfs dominate for both late and early types. On the other hand, early-type dwarfs in our sample tend not to be in isolated environments, while the late types tend to be in equal proportions in terms of the D_{host} parameter threshold.

5.3. Photometric Results

In this section, we present several results derived from the analysis performed with the photometric data already described in Sections 4.1 and 4.2, and how they compare to the public results given in the NSA Catalog. The images and profiles for all the galaxies in our sample used to derive the results in this section are available as part of the SDSS-IV MaNDala VAC (for details, we refer to the Appendix).

5.3.1. Comparison with NSA

To ensure that our photometric analysis is consistent with previous results, here we present a series of comparisons between our results and those available in the NSA Catalog. We recall that our analysis is based on the photometry from the DESI Legacy Imaging Surveys, while in the NSA Catalog, the shallower SDSS photometry has been used.

In the upper panels of Figure 5, we show the comparisons of the Sérsic index and R_e ²⁵ derived from our photometric analysis and Sérsic fit in the r -band versus those given in the NSA Catalog.²⁶ In both plots, we see a good agreement with the NSA results. However, in both cases, when reaching the largest values, the dispersion in the points becomes larger. In the case of the index n , it is noticeable that, for the largest values reported by the NSA ($n_r > 2$), we find smaller values, mostly between 1 and 2, which are more consistent with smaller and LTG galaxies. The opposite occurs in the case of R_e , for which, in general, our estimations seem to be larger than those reported in the NSA. These panels both exhibit some outliers. We checked if the large differences between the Sérsic indices and R_e derived by us and those reported in the NSA Catalogue for those objects may be due to bad fits of the SB profiles; however, the majority of them have χ^2 values below 3 for both plots. A possible source of the differences could be the fact that the NSA fits use an extrapolation while ours use only observed points with the SB profiles.

In the two bottom panels of Figure 5, we show the comparisons between our estimations of the apparent magnitudes in the g , r , and z bands versus those from the NSA Catalog. The NSA apparent magnitudes were derived using the absolute ones retrieved directly from their catalog. In all panels, we also include the Pearson correlation coefficient (r). As in the previous plots, in general there is a good agreement, in

²⁵ Sérsic_TH50 column reported in their public catalog.

²⁶ The Sérsic_TH50 column in their public catalog.

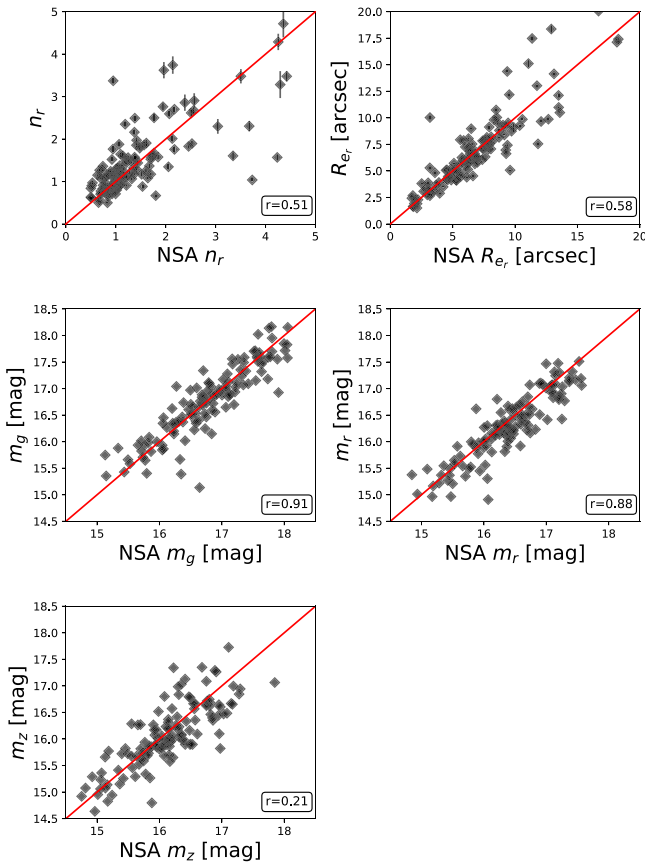


Figure 5. Comparisons of the principal results from our Sérsic fit against those previously presented in the NSA Catalog. From the top to the bottom panels, we show the following comparisons: Sérsic index and effective radius in the r band, and apparent magnitudes in the g , r , and z bands. The red line shows the one-to-one relation. In all panels, the Pearson correlation coefficient is shown.

particular in the g and r bands, while for the z band, the dispersion seems larger, which is also visible in its low r value.

Also, Arora et al. (2021) recently performed a photometric analysis for 4585 MaNGA galaxies using DESI data. For the 71 galaxies that we have in common with their sample, we performed comparisons for some global properties provided by them, such as apparent magnitudes, R_e , and μ_{eff} , and our results are consistent with theirs (Pearson coefficients of ~ 0.9 for the first two and ~ 0.8 for the last one). It is important to mention that the results given by Arora et al. (2021) are not based on Sérsic fits; instead, they are taken directly from the photometric analysis, meaning that these comparisons are not direct.

5.3.2. Radial Surface Brightness and Color Profiles

In the left panels of Figure 6, we show the individual SB profiles for all the galaxies in our sample in the g , r , and z bands (for each band, the radii are normalized to their corresponding R_e derived from the Sérsic fit). On top of them, an average profile is shown for each band. In dashed lines and shaded areas, the mean depth limits for each band of the MaNDala sample and the standard deviations are shown, respectively (see Section 4.2 for the details of their derivations). For comparison, the red solid line shows the SDSS depth limit in the r band at $24.5 \text{ mag arcsec}^{-2}$ (see, for example, Strauss et al. 2002), which emphasizes the difference in photometric depth achieved by DESI and SDSS image data. These plots give an idea of the difference between the photometric depths

of the DESI data in the three bands. We can see that the flattening of the average profile rises to brighter SB values when moving from the g to the z band. This is relevant because the flattening of these profiles is related to the radius of the galaxies in which the brightness of the sky is starting to dominate in the data. For the g band, we are able to obtain the best SB profiles, as on average, they arrive out to $\sim 5 R_e$ before the profiles start to flatten. The flattening moves to inner regions of the galaxies when moving to redder bands, as it occurs at $\sim 4.5 R_e$ and $\sim 3.5 R_e$ in the g and z bands, respectively (note that, as shown in Figure 7 below, the measured effective radii are roughly similar in the three bands). It is also important to mention that NSA SB profiles for these galaxies can extend to larger radii, beyond the photometric depth limits of the SDSS images (see middle left panel of Figure 6). In contrast, the profiles from our analysis naturally extend beyond the SDSS depths up to the DESI limits, showing the shapes of the profiles obtained at those radii.

In order to make evident any systematic difference provided by the morphology, in the top right panel of Figure 6, we reproduce the profiles in the r band of the top left panel of the same figure, but color-coded according to the morphology: red and blue for the early and late types, respectively. In a second panel, we also show the individual color $g - r$ profiles for our sample, color-coded in the same way as in the previous panel. On top of both panels, a median profile is shown in magenta for the early-type galaxies and in dark blue for the late ones. These general profiles are derived binning the early and late types' distributions with a bin size of 0.4 in units of R_e and calculating the median value for each one. The error bars correspond to the 16th–84th percentiles of the distributions within each bin.

According to the right panel of Figure 6, the r -band SB profiles of the dwarf LTGs are less scattered than those of the dwarf ETGs (note that the distributions of magnitudes or masses of both subsamples are roughly similar, and given that LTGs are much more numerous than ETGs, the greater dispersion of the latter with respect to the former is hardly an effect of sample size). On average, the ETGs have slightly higher SB at all radii than the LTGs. As for the $g - r$ color gradients, they fluctuate with radius but around a fixed value; that is, they tend to be flat or slightly positive, both for dwarf LTGs and ETGs. As expected, the latter are redder than the former.

5.3.3. Photometric Characterization of the Sample

Making use of our photometric results, we can now perform a basic characterization of the MaNDala sample, such as identifying its limits, and even testing if all the objects are consistent with the expected behavior for DGs.

Histograms of the Sérsic index, effective radius, apparent and absolute magnitudes, central SB, central color, and color gradients for the three DESI photometric bands used in this work for our sample are shown in Figure 7. Color gradients are defined as

$$\nabla(\lambda_1 - \lambda_2) = \frac{\Delta(\lambda_1 - \lambda_2)(R)}{\Delta(\log R)}. \quad (7)$$

We evaluate $\nabla(\lambda_1 - \lambda_2)$ at 0.1 and $1 R_e$. All of these properties are results of the Sérsic fits explained in Section 4.2.1. These distributions show the natural limits of the sample in brightness, which are summarized in Table 1, along with other

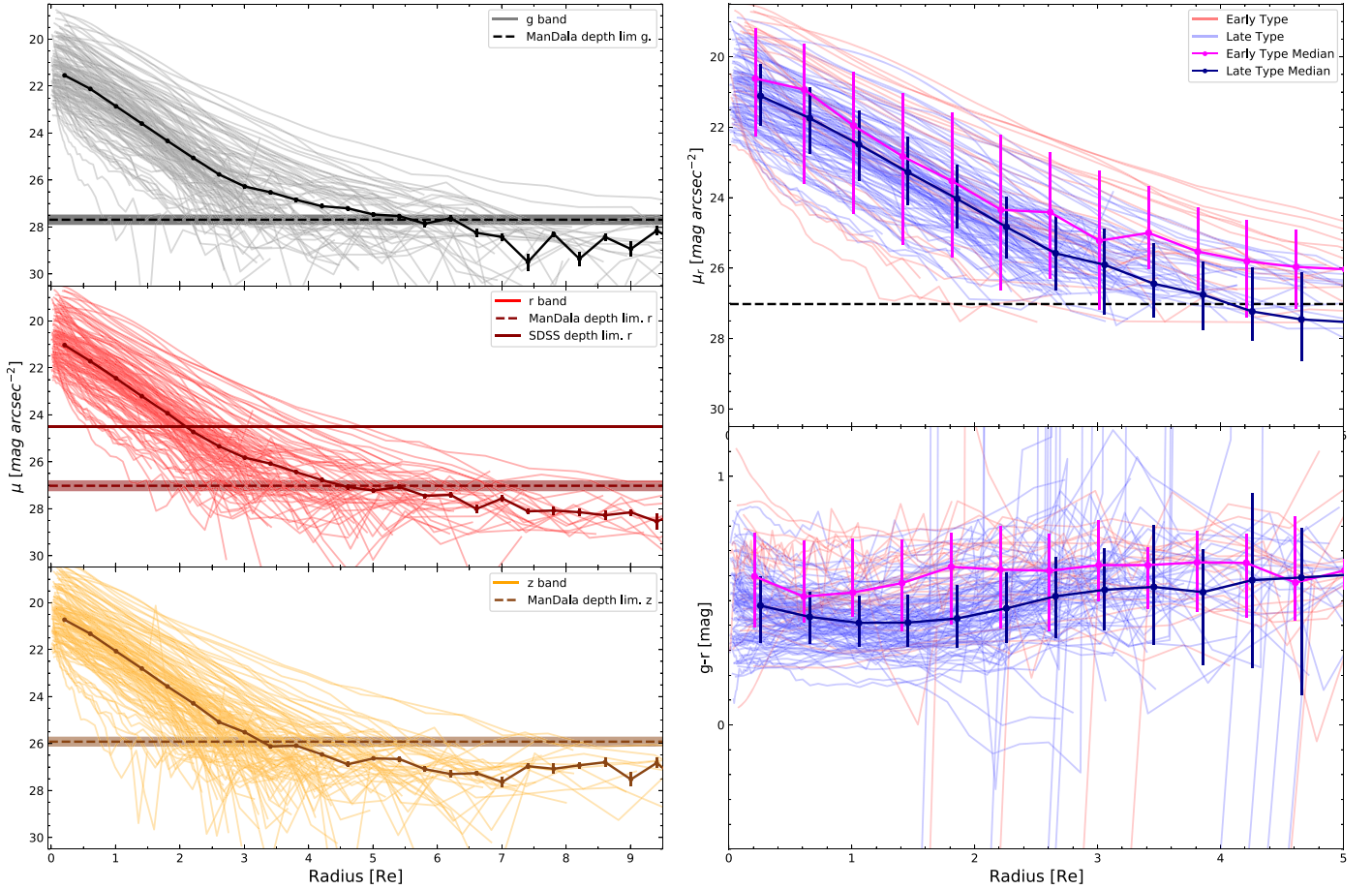


Figure 6. Left panels: from the uppermost to the bottom, the individual surface brightness profiles for all the MaNDala galaxies, in the g , r , and z bands, respectively. On top of them, an average profile is shown, calculated in radial bins of $0.4 R_e$. The dashed lines represent the mean depth limit values for the galaxies in the sample for each band, while 1σ of those values are shown by the shaded areas around them. Right panels: on the top are shown the same surface brightness profiles for all the MaNDala galaxies in the r band, as in the right panel, with their depth limits shown as dashed lines, but color-coded in terms of morphology (blue for late types and red for early types). In the bottom panels, the $g - r$ profiles for each MaNDala galaxy are shown, with the same color code as in the top panels. On top of both panels, the median profiles for early- and late-type galaxies are plotted in magenta and dark blue, respectively, with error bars representing the 16th and 84th percentiles. The surface brightness and color profiles shown in this figure are cut according the individual depth limit for each galaxy.

relevant characteristics. In general, we can see that the MaNDala sample is indeed biased toward bright DGs, as suggested by the M_* distribution shown in Figure 1. Moreover, the dashed magenta line in the absolute magnitude histogram represents the limit imposed to select the galaxies in our sample (NSA $M_g > -18.5$). It is noticeable that a few of our galaxies surpass this limit while using the results derived with the DESI photometry and with our Sérsic fits, and as shown in the previous section, some galaxies tend to give brighter magnitudes when compared with those available in the NSA Catalog.

From Figure 7, we see that the Sérsic index of dwarf ETGs tends to be higher and with a greater spread than for LTGs (there is also a small trend of lower n values as the band is redder, especially for ETGs). As reported in Table 1, the medians of n_r for ETGs and LTGs are 2.50 and 1.15, and the 1σ scatters are 1.60 and 0.94, respectively. A similar trend is observed for μ_0 : ETGs tend to have higher central SBs and a greater spread than LTGs (median $\mu_{0,r}$ of 16.98 and 20.23 mag arcsec $^{-2}$, respectively). Regarding the sizes, R_e depends little on the photometric band and tends to be smaller for the ETGs than for the LTGs (note that the absolute magnitude distributions are similar for both groups): the median $R_{e,r}$ are 1.33 and 2.58 kpc,

respectively. In general and as expected, the dwarf ETGs are significantly more compact than the dwarf LTGs; the ratio of the median r -band luminosity to the median effective radius for ETGs is ≈ 1.7 times higher than for LTGs. As for the colors, ETGs are redder on average than LTGs (medians of $g - r$ of 0.57 and 0.44 mag, respectively) but with a broader distribution. Finally, the $g - r$ color gradients of the MaNDala galaxies oscillate around 0, meaning that the gradients are nearly flat.

Using the ellipticity profiles derived from our analysis, we can interpolate the ϵ value at any radius in the r band. In particular, we can also interpolate an approximation of the radius that contains 90% of the light (r_{90}), using the cumulative flux profiles for each galaxy (upper right panel in Figure 3), and then interpolate the ϵ at that radius for all the galaxies in the sample. Assuming these values as the overall ellipticities for the galaxies, they can be converted into inclinations ($\cos i = b/a$). The MaNDala sample has galaxies with various inclinations, with a mean of $53^{\circ}83$ ($\epsilon_{\text{mean}} = 0.43$): 18 galaxies ($\sim 13\%$ of the sample) are highly inclined, $i > 70^{\circ}$ ($\epsilon \sim 0.66$), while 14 ($\sim 10\%$ of the sample) exhibit low inclinations, $i < 30^{\circ}$ ($\epsilon \sim 0.13$). Recall that cuts were applied to derive all the profiles, including the cumulative flux one, which means that the r_{90} may be underestimated.

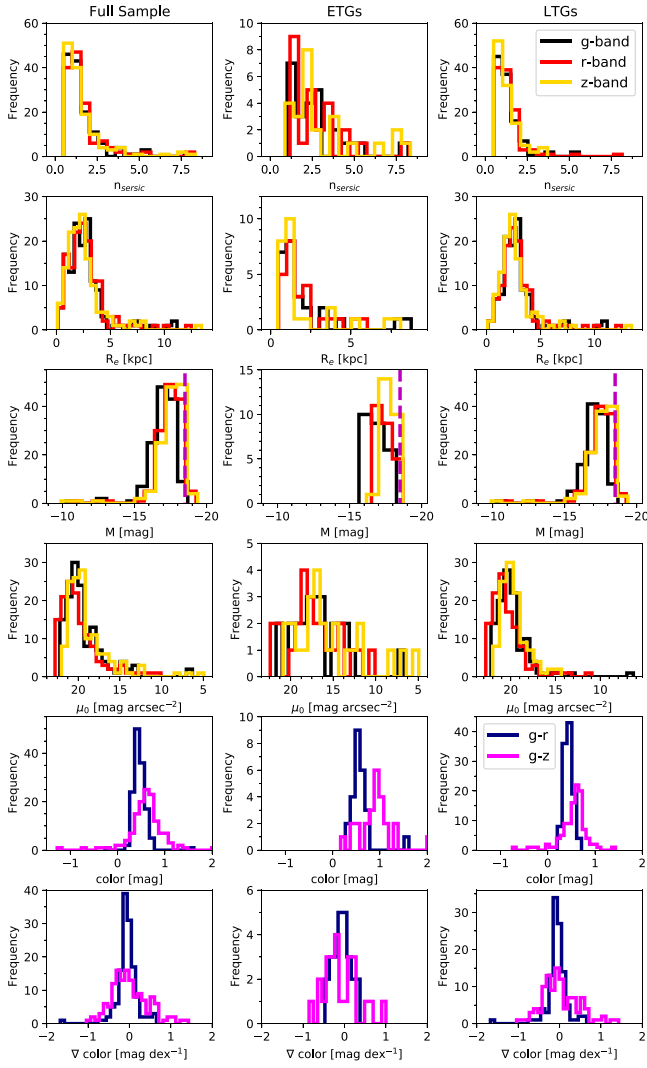


Figure 7. Set of histograms that characterize the full MaNDala sample (left column), the early-type galaxies (middle columns), and the late-types (right column). From the uppermost to the bottom, the panels show the distributions of the following properties: Sérsic index, effective radius, apparent magnitude, absolute magnitude, central surface brightness, color measured at the center, and color gradients measured between 0.1 and $1 R_e$. The color code is the same used to present the surface brightness and color profiles in Figure 3. The magenta dashed line in the absolute magnitude panel marks the $M_g = -18.5$ mag limit imposed to select this sample, used with the NSA Catalog photometric data.

In Figure 8, we show the relation between the mean effective SB (Graham & Driver 2005), which is defined as

$$\langle \mu_e \rangle = m + 2.5 \log_{10}(2\pi R_e^2), \quad (8)$$

and the $g-r$ color and the color gradient $\nabla(g-r)$ as well. To calculate $\langle \mu_e \rangle_g$, we use our estimations of the Sérsic apparent magnitude in g , and the R_e estimated in the g band. There is no significant trend of the $g-r$ color with $\langle \mu_e \rangle_g$, neither for ETGs nor for LTGs. We use crosses and diamonds to indicate field and group dwarfs, respectively. There is no clear segregation in this plot, due to environmental characterization; however, the highest-SB dwarfs in the sample are all ETGs in denser environments, $D_{\text{host}} \leq 1$ Mpc. Regarding the $g-r$ gradient, for the dwarfs with $\langle \mu_e \rangle_g < 22$ (high SBs), positive gradients are more common, while for those with lower SBs, flat or negative

Table 1
Statistical Parameters of the Photometric Properties in the r Band of the MaNDala Sample and for the $g-r$ Colors and Color Gradients^a

	Max	Min	Mean	Median	σ
Full sample					
n_r	8.30	0.50	1.64	1.25	1.22
R_{e_r} [kpc]	12.49	0.15	2.71	2.45	1.76
m_r [mag]	17.61	12.28	16.18	16.27	0.87
M_r [mag]	-10.63	-19.27	-17.38	-17.48	1.05
μ_{0_r} [mag arcsec ⁻²]	22.20	6.30	19.29	19.98	2.58
$g-r$ [mag]	1.61	-0.27	0.46	0.44	0.16
$\nabla(g-r)$ [mag dex ⁻¹]	0.66	-1.67	-0.05	-0.06	0.25
Early Types					
n_r	8.30	1.18	2.77	2.50	1.60
R_{e_r} [kpc]	6.02	0.48	1.93	1.33	1.46
m_r [mag]	17.61	15.16	16.44	16.32	0.59
M_r [mag]	-16.52	-18.69	-17.40	-17.26	0.57
μ_{0_r} [mag arcsec ⁻²]	21.71	6.64	16.63	16.98	3.15
$g-r$ [mag]	1.61	0.27	0.59	0.57	0.24
$\nabla(g-r)$ [mag dex ⁻¹]	0.38	-0.47	-0.05	-0.07	0.20
Late Types					
n_r	8.15	0.50	1.38	1.15	0.94
R_{e_r} [arcsec]	12.49	0.15	2.91	2.58	1.79
m_r [mag]	17.51	12.28	16.14	16.24	0.88
M_r [mag]	-10.63	-19.27	-17.42	-17.53	1.02
μ_{0_r} [mag arcsec ⁻²]	22.20	6.30	19.89	20.23	2.00
$g-r$ [mag]	0.71	0.20	0.44	0.44	0.10
$\nabla(g-r)$ [mag dex ⁻¹]	0.66	-1.67	-0.06	-0.06	0.26

Note.^a The statistics for the early- and late-type subsamples are also presented for the 135 galaxies for which we have morphological information.

gradients are more common. There is no clear segregation due to environment.

A classical way to characterize dwarfs is using the so-called Kormendy relations (Kormendy 1977, 1985), which relate galaxy parameters that can be inferred by a Sérsic fit. In Figure 9, we show one of these relations, which compares the absolute magnitude in the g band and R_e in the same band. In this plot, we aim to locate the MaNDala sample within a summary similar to the one presented by Poulain et al. (2021), which compares several DG samples (Poulain et al. 2021; Ferrarese et al. 2020; Carlsten et al. 2020; Eigenthaler et al. 2018), and some Ultra Diffuse Galaxy (UDGs) samples (Lim et al. 2020; van Dokkum et al. 2015). Along with these samples, we present results for normal (giant) early- and late-type galaxies represented with solid red and blue lines. Effective radii were obtained from the Meert et al. (2013, 2016) catalogs based on the SDSS DR7 and the morphologies from the Huertas-Company et al. (2011) catalog. We compute these relations for galaxies with spectroscopic redshifts $z \leq 0.07$ in order to avoid biases due to the PSF resolution of the SDSS. The g -band magnitudes were K-corrected and evolution-corrected to $z=0$ following Dragomir et al. (2018) and Rodríguez-Puebla et al. (2020b). We see that our sample populates the brighter end of the distribution for DGs, indicating that these objects are indeed bright DGs, with the exception of a few galaxies that fall below and within the cloud of DGs for magnitudes fainter than -16 . For a given M_g , the radii of our early-type dwarfs agree with the low-luminosity end of the Meert et al. (2013, 2016) catalogs of normal ETGs, though the former have a very large scatter. For our late-type

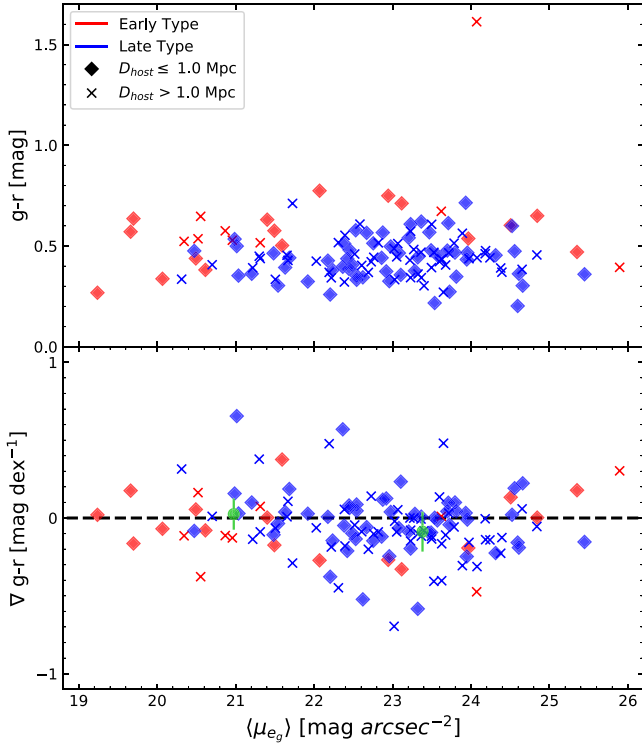


Figure 8. Color and color gradients in the top and bottom panels, respectively. Both panels are color-coded according to morphology types, red for early-types and blue for late-types. Symbols correspond to environment, where diamonds represent galaxies with $D_{host} \leq 1.0$ Mpc and crosses galaxies with $D_{host} > 1.0$ Mpc. Green points in the bottom panels represent the mean $\langle \mu_{e,g} \rangle$ and $\nabla(g-r)$ values for all galaxies below and above 22 mag arcsec $^{-2}$ in $\langle \mu_{e,g} \rangle$, and error bars represent their standard deviation.

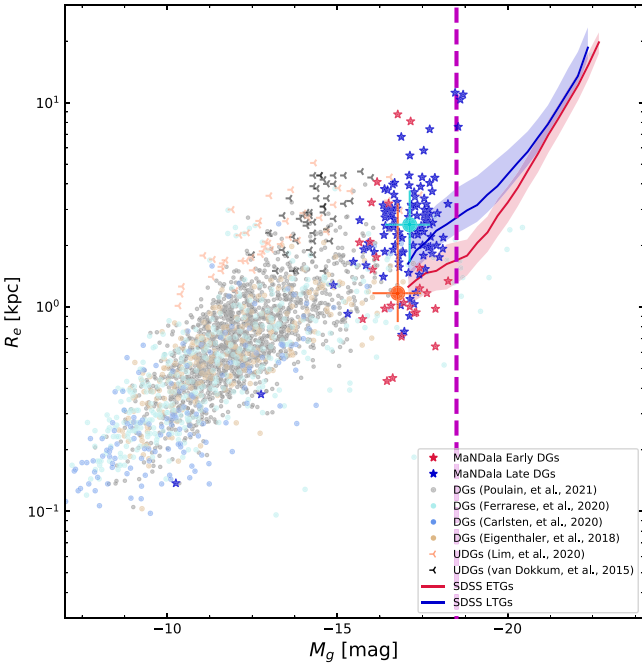


Figure 9. The g -band absolute magnitude vs. g -band effective radius of the MaNDala sample, separated into LTG and ETG dwarfs (blue and red stars, respectively). The large blue and red circles with error bars are the respective running median and 16–84th percentiles. For the purpose of comparison, other samples of DGs are plotted (see the sources in the inset). The magenta dashed line marks the $M_g = -18.5$ mag limit imposed to select this sample, using the NSA Catalog photometric data.

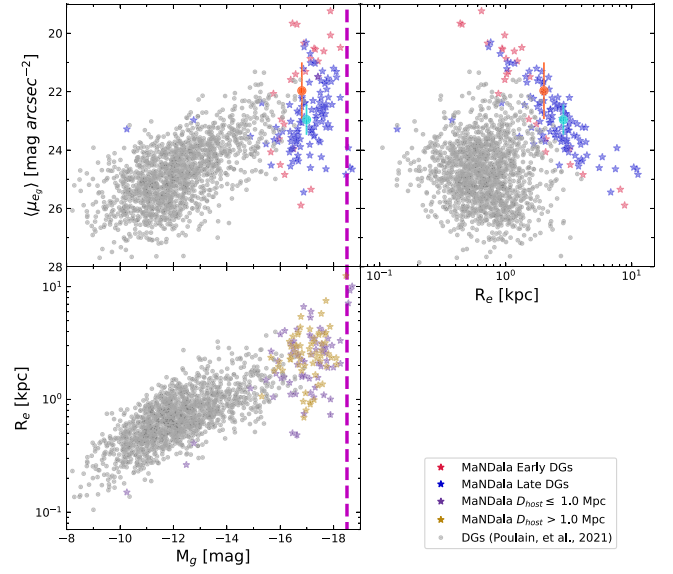


Figure 10. Kormendy's diagrams for the MaNDala sample in the g band, compared with the Poulain et al. (2021) dwarf galaxy sample. In the upper panels, our galaxies are color-coded to represent the two morphology groups present in the sample: red for early-types and blue for late-types, while the red and blue circles represent their means, and the error bars indicate their respective 1σ . In the bottom panel, the color code represents the environment: dark yellow for dwarfs with $D_{host} \leq 1.0$ Mpc and purple for those with $D_{host} > 1.0$ Mpc. In the left-side panels, magenta dashed lines mark the $M_g = -18.5$ mag limit imposed to select this sample, using the NSA Catalog photometric data.

dwarfs, they tend, on average, to have larger radii than the low-luminosity end of normal LTGs. In particular, there is a fraction of MaNDala galaxies with very large radii, $R_e > 3$ kpc, for their luminosities. They appear as an extension to higher magnitudes of the UDCs depicted in this figure. In general, our results show that the $R_e - M_g$ relation tends to flatten, especially for LTGs, in the range $-19 \leq M_g < -15$, though with a large scatter.

In Figure 10, we present the full Kormendy diagrams for the g band. For the purpose of comparison, we present along with the MaNDala sample the ones described in Habas et al. (2020) and Poulain et al. (2021), with gray dots. In the upper panels, the relations between $\langle \mu_e \rangle$ and absolute magnitude M_g (left panel) and R_e (right panel) are presented. In the left plot, in general terms, the mean SB increases for brighter galaxies, which is visible as our sample continues the tendency drawn by the Poulain et al. (2021) sample. However, those low-SB galaxies with $\langle \mu_{e,g} \rangle \gtrsim 24.5$ mag arcsec $^{-2}$ are outliers in this relation. These galaxies may be so-called UDGs,²⁷ and we have already noticed them in the $R_e - \langle \mu_e \rangle$ diagram shown in Figure 9. Note also that our dwarf ETGs have, on average, smaller radii and higher mean effective SBs than the dwarf LTGs, while their magnitudes are similar. As for the right-side plot, most of the MaNDala galaxies lie in a diagonal band, where for larger R_e , the $\langle \mu_{e,g} \rangle$ becomes lower. According to Equation (8), this is due to the short range in absolute magnitudes of our sample. However, comparing the MaNDala sample against a larger and less luminous sample, such as the one given by Poulain et al. (2021), makes it easier to understand that MaNDala is an extension of this sample to

²⁷ Poulain et al. (2021), following the definition of UDGs by van Dokkum et al. (2015), find that the g -band effective SBs of UDGs are larger than ≈ 24.5 mag arcsec $^{-2}$.

larger/brighter dwarfs. In any case, there are dwarfs that seem to be outliers from the main trend, i.e., those with $\langle\mu_{e,g}\rangle \gtrsim 24.5$ mag arcsec $^{-2}$ and $R_e \gtrsim 1.5$ kpc (these are roughly the criteria to define UDGs; see Poulain et al. 2021; van Dokkum et al. 2015). These galaxies also seem to be outliers in the $M_g - \langle\mu_e\rangle$ and $M_g - R_e$ diagrams, and as mentioned above, they may be UDG candidates. Note also that there are a few MaNDala galaxies that strongly deviate from the main trend, but at the other extreme, there are those with high SBs and small radii for their luminosity, i.e., very compact objects. These are mainly ETG dwarfs.

We can analyze the details of the individual galaxies that lay in the two already identified outlier groups. Starting with the UDG candidates, we find 12 galaxies that fulfill the aforementioned conditions ($\langle\mu_{e,g}\rangle \gtrsim 24.5$ mag arcsec $^{-2}$ and $R_e \gtrsim 1.5$ kpc). However, five of them have reduced χ^2 values for their g -band Sérsic fit larger than 2.5; this leads to think that their location in the Kormendy diagram may be inaccurate. Another galaxy of this group exhibits a small χ^2 value of its g -band fit (of 0.6), which may also indicate that this fit may not be optimal. The remaining six galaxies could be considered as UDG candidates. Four of them, manga-8487-9101, manga-9494-6103, manga-9876-12704, and manga-10517-12704, exhibit early-type morphologies; however, the last two show a clearly bright center. The other two, manga-10221-12704 and manga-10841-12705, have late-type morphologies. However, the last one shows signs of interaction. On the other hand, to select the MaNDala galaxies with large $\langle\mu_e\rangle$ values and small radii, we impose an arbitrary limit of $\langle\mu_e\rangle \leq 20$ mag arcsec $^{-2}$. Only three galaxies surpass this limit; however, one of them also have χ^2 values for their g -band Sérsic fit larger than 2.5. For the remaining two (manga-8727-3702 and manga 9495-1901), their χ^2 values are close to unity (~ 0.8) and we can assume they are indeed very compact and bright DGs.

The lower panel of Figure 10 is similar to Figure 9, but indicating now the field/group information for our sample. As can be seen, there is not a clear segregation of the MaNDala galaxies by this environmental characterization in the $M_g - R_e$ diagram. We have verified that this segregation does not appear in the other diagrams either. We also do not observe a notable segregation between central and satellite dwarfs.

Finally, in Figure 11, we locate the MaNDala galaxies in the $M_* - R_e$ diagram, shown as stars (color-coded according to their morphological type as in Figures 9 and 10), along with all the DGs in the NSA Catalog, selected with the same criteria as the ones in our sample. The resulting 25,998 NSA galaxies are traced by gray contours. The vast majority of the MaNDala galaxies are within the 1σ distribution of the NSA Catalog. In solid lines, we show two of the mass–size relation fits reported by Nedkova et al. (2021), corresponding to quiescent and star-forming galaxies in red and blue respectively (in Section 5.4, we will show that almost all the LTG dwarfs are star-forming). Both fits were derived for galaxies in a redshift range of $0.2 < z < 0.5$, and for the entire range of M_* considered in their sample ($10^7 M_\odot < M_* < 10^{11.6} M_\odot$). We also show the fits provided by Lange et al. (2015) for ETGs and LTGs from the GAMA local survey, using their morphology cut, in red and blue dashed lines, respectively. In addition, we compare to the $M_* - R_e$ relationship derived from the effective radii reported in Meert et al. (2013, 2016) catalogs (as in Figure 9) and the stellar masses for this survey as derived in Rodríguez-Puebla et al. (2020b). All the plotted mean relations agree well with

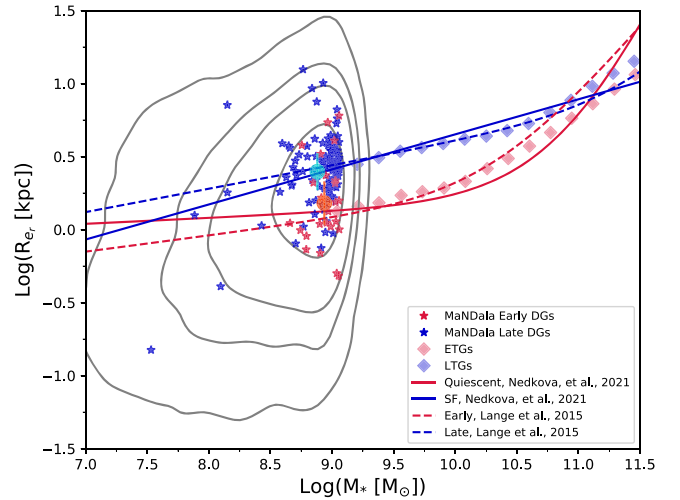


Figure 11. Location of the MaNDala galaxies in the mass–size relation (in red and blue stars for ETGs and LTGs, respectively; their averages are shown by the red and blue circles, while the error bar shows 1σ of their distribution). For comparison, the contours underneath trace the location of all the NSA DGs that fulfill the same selection criteria as our sample (from the innermost to the outermost, they represent: 0.5σ , 1σ , 1.5σ , and 2σ of this data set). The solid lines are the fits reported for this relation by Nedkova et al. (2021) for quiescent and star-forming galaxies in red and blue, respectively. The dashed lines are also fits reported by Lange et al. (2015) for early- and late-type galaxies, respectively. Diamonds in red and blue show a comparison of higher-mass galaxies with derivations for the R_e given by Meert et al. (2013, 2016) and for the M_* by Rodríguez-Puebla et al. (2020b).

our results for the MaNDala galaxies, both for LTGs and ETGs. On average, the former are larger than the latter at a given stellar mass.

5.4. Spectroscopic Results

In this section, we present results of global properties related to the stellar populations and emission lines of the MaNDala galaxies, obtained from the spectroscopic analysis described in Section 4.3. The galaxy properties displayed in this section are available as part of the SDSS-IV MaNDala VAC (see the details in Appendix). We leave it for a series of future articles to explore the evolutionary and spatially resolved results of the fossil record analysis that can be derived using the MaNGA data.

5.4.1. Ionized Gas Results

In Figure 12, we present the Baldwin–Philips–Terlevich N II diagram (BPT; Baldwin et al. 1981) for the MaNDala galaxies, using the corresponding emission line fluxes integrated within the FoV of each galaxy. The BPT diagram, as well as other line diagnostic diagrams (Veilleux & Osterbrock 1987; Kewley et al. 2001), are used to distinguish the ionization mechanisms of nebular gas, which can be associated with active galactic nuclei (AGN), SF, or hot old stars. Based on the BPT–N II diagram and on the $H\alpha$ EW, we attempt a classification of the SF activity level of MaNDala galaxies, following the criteria discussed in Sánchez et al. (2014), Cano-Díaz et al. (2016), and Cano-Díaz et al. (2019). Three types of galaxies are defined:

1. Star-forming (SFg), those with $EW(H\alpha) > 6 \text{ \AA}$ and below the Kewley line (black solid line in Figure 12; Kewley et al. 2001);

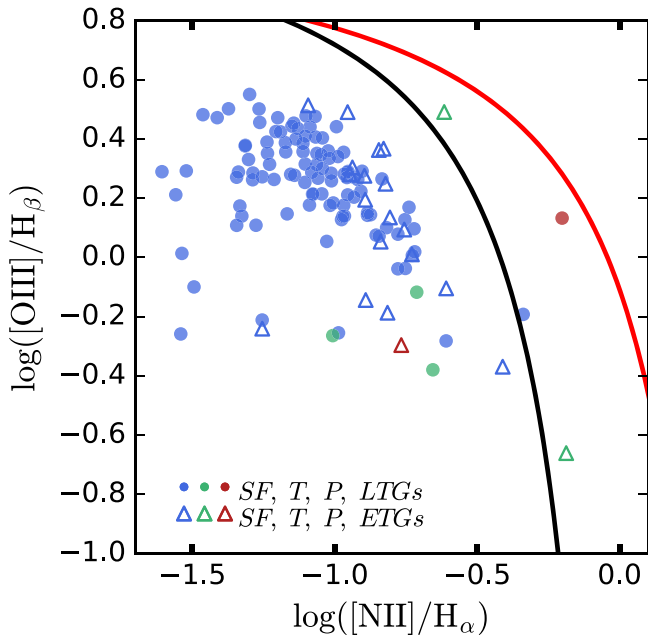


Figure 12. The BPT-N II diagram for the MaNDala galaxies reported in this paper. The line intensities are integrated within the FoV of each galaxy. The blue, green, and red colors refer to our classifications of Star-forming (SFg), Transitioning (T), and Passive (P) galaxies, respectively, while closed circles and open triangles are for the LTG and ETG dwarfs, respectively. The lines indicate different criteria to identify the level of SF and AGN activity: the red line indicates the Kewley criteria (Kewley et al. 2001), and the black line indicates the Kauffmann criterion (Kauffmann et al. 2003).

2. Passive (P; also referred to as quiescent, quenched, or retired), those with $\text{EW}(\text{H}\alpha) < 3 \text{ \AA}$ independently of their position in the BPT diagram; and
3. Transitioning (T), those with $3 \text{ \AA} \leq \text{EW}(\text{H}\alpha) \leq 6 \text{ \AA}$.

Applying the above criteria, we find that 115 galaxies (92%) are SFg, five are P galaxies (4%), and five are T (4%). The blue, red, and green symbols in Figure 12 show the SFg, P, and T galaxies, respectively, while closed circles and open triangles are for the LTG and ETG dwarfs, respectively. In Figure 12, only two P galaxies are plotted. This is because the $\text{H}\alpha$ and $[\text{OIII}]$ lines of the other three P galaxies are very low, such that the line ratios for them are well outside the ranges of the axes. It can be definitively stated that the great majority of our DGs in the MaNGA sample have signatures of being SFg. Among the dwarf LTGs, 96% are SFg, 2% are T, and 2% are P. For the dwarf ETGs, these fractions are 75%, 12.5%, and 12.5%, accordingly. Thus, even for the ETGs, most of the dwarfs are SFg galaxies. On the other hand, we did not find significant signatures of AGN in any MaNDala galaxy when using the BPT diagram; however, further and more detailed analysis is required in order to exclude the possibility of finding nuclear activity in any MaNDala galaxy, as previous studies of dwarf galaxies observed in MaNGA have found AGN signatures (Mezcua & Domínguez Sánchez 2020; Penny et al. 2018, with samples selected to have galaxies with: $M_* < 3$ and $5 \times 10^9 M_\odot$, respectively). In summary, most of dwarf galaxies in the MaNGA survey are SFg without signatures of AGN contribution. In Section 5.4.3, we will explore the $\text{SFR}-M_*$ relationship and show that our DG sample is a low-mass extension of the main sequence of SFg galaxies.

5.4.2. Properties of the Stellar Populations

We use the (mass- and luminosity-weighted) stellar age and metallicity maps based on the SPS analysis from PYPipe3D described in Section 4.3 to estimate the respective (mass- and luminosity-weighted) integrated ages and metallicities: Age_{mw} , Age_{lw} , $Z_{*,\text{mw}}$, and $Z_{*,\text{lw}}$, for each MaNDala galaxy. We also use the index maps to obtain the integrated D4000 index, defined as the ratio between the continuum flux within 4050–4250 Å and 3750–3950 Å (Sánchez et al. 2016b). In the VAC, the above quantities are reported within the FOV and R_e for each individual galaxy, but in the present work, unless otherwise specified, we present these results within the FOV.

The two upper left panels of Figure 13 show Age_{mw} and Age_{lw} versus M_* , respectively, for our DG sample (averaging of the SSPs’ ages is logarithmic, see Section 4.3). The colors and symbols are as in Figure 12. The isodensity contours in the same figure present the results for the whole MaNGA sample. As for M_* , we use the masses from the NSA catalog. The masses calculated with PYPipe3D from the MaNGA data cubes are, on average, slightly lower than those from the NSA catalog, after passing to the Chabrier IMF; this may be due to aperture effects. For a more detailed discussion, see Sánchez et al. (2022).

According to the left panels in Figure 13, low-mass galaxies, and dwarfs in particular, show a wide range of mass-weighted ages, the latter with a median of 6.2 Gyr and 16th–84th percentiles of 7.1–4.2 Gyr; see the right panel for the full distribution. On average, these ages are slightly lower than those of the massive galaxies in the MaNGA survey. The situation is different for the light-weighted age: dwarfs have much lower ages than massive galaxies, and with a small scatter. The median and 16th–84th percentiles of Age_{lw} are 0.4 and 0.6–0.3 Gyrs, respectively. The few dwarfs with $\text{Age}_{\text{lw}} > 1$ Gyr are passive or in transition. Unlike Age_{mw} , which has a similar distribution for dwarf LTGs and ETGs, the values of Age_{lw} for dwarf ETGs tend to be larger than those for dwarf LTGs. The lower left panel of Figure 13 shows the logarithmic differences of the mass- and light-weighted ages for the MaNDala and the whole MaNGA samples. For massive galaxies, this difference is on average small, with a median of 0.18 dex. For the dwarfs, however, the differences are very large, with a median of 1.15 dex, and with a large scatter; see the right panel for the full distribution. The differences are smaller on average for dwarf ETGs than for the LTG ones. The mass-weighted age is biased toward older stellar populations, which informs us about when a significant fraction of the stellar mass was formed, while the light-weighted age is more sensitive to late episodes of SF. Therefore, the difference between Age_{lw} and Age_{mw} can be indicative of how coeval or dispersed in time the SFH of a galaxy was, or it can also indicate the presence of very recent bursts of SF, as is the case of poststarburst galaxies (Plauchu-Frayn et al. 2012; Lacerna et al. 2020; Ge et al. 2021). If the difference is very large, it indicates that there are two markedly different populations in the SSP decomposition of the observed spectrum: one that formed early and is dominant in the total stellar mass, and another associated with late SF episodes, with a low contribution to the total mass. With age differences as large as factors of 3–30, this seems to be the case for the MaNGA dwarfs.

In the right panels of Figure 13, we show the stellar mass–metallicity relationships, both for $Z_{*,\text{mw}}$ and $Z_{*,\text{lw}}$, for the dwarf

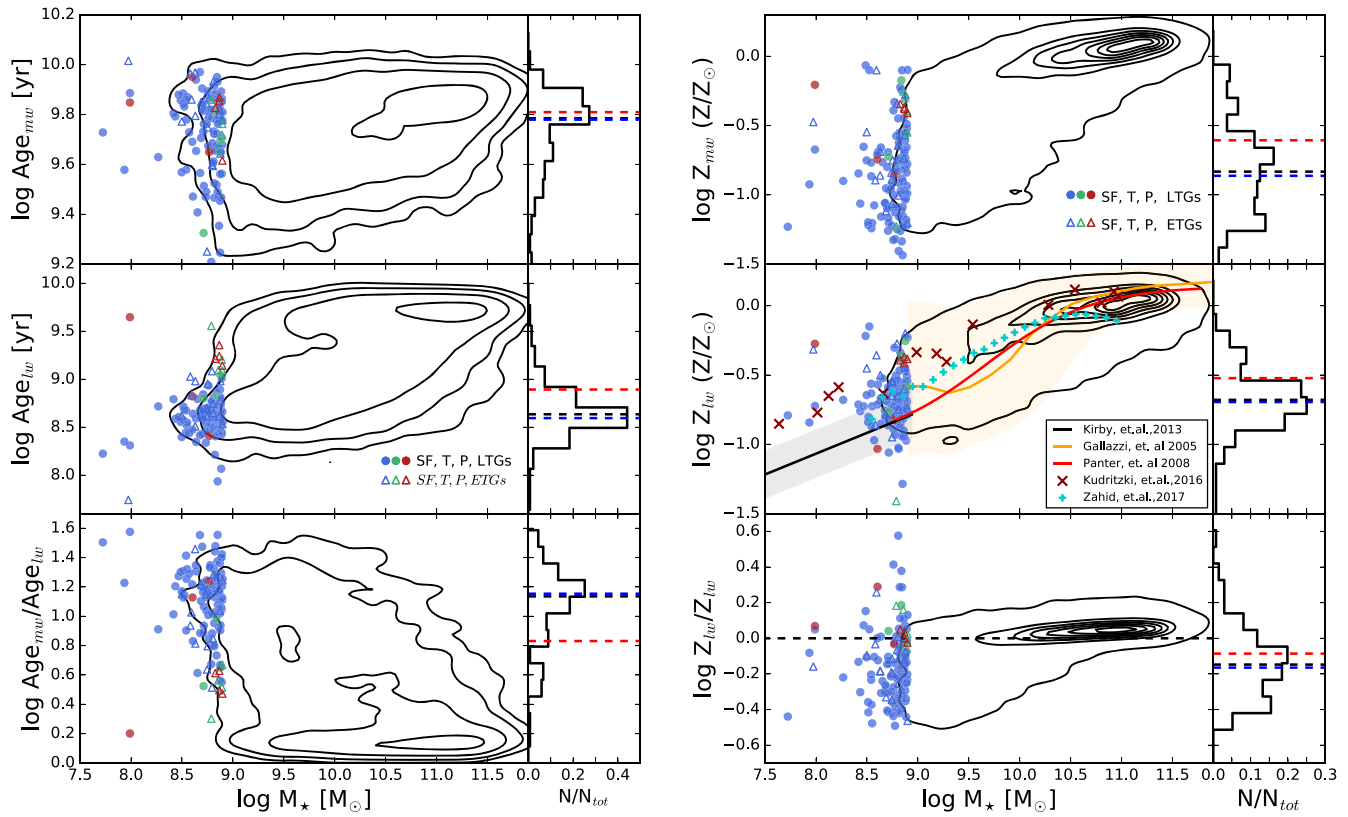


Figure 13. Left panels: Stellar mass–age relations for the MaNDala galaxies (symbols) and the whole MaNGA sample (isodensity contours). The ages are defined within the FoV of each galaxy, while for M_* , we used the NSA catalog. The upper and middle panels show the mass- and luminosity-weighted ages, respectively, while the lower panels show the logarithms of their ratios. The colors and symbols are as in Figure 12. The isocontours enclose 99%, 96%, 84%, and 37% of the data (no correction for volume completeness was applied). Their right inset panels show the distributions of $\log \text{Age}_{\text{mw}}$, $\log \text{Age}_{\text{lw}}$, and $\log (\text{Age}_{\text{mw}}/\text{Age}_{\text{lw}})$ for the MaNDala galaxies. The black dashed lines indicate the respective medians, while the blue and red dashed lines correspond to medians of the LTG and ETG subsamples, respectively. Right panels: Same as left panels, but for the mass- and light-weighted stellar metallicities. The isocontours in this case enclose 97%, 61%, 45%, 33%, 23%, 13%, and 5% of the data (no correction for volume completeness was applied). In the middle panel, we have added determinations from several previous studies, as indicated in the inset box (see text).

and whole MaNGA samples; the right panels show the respective metallicity distributions. Both the mass- and light-weighted stellar metallicities of dwarfs are significantly lower than those of massive galaxies, as many previous works have shown (e.g., Ikuta & Arimoto 2002; Hidalgo 2017; McQuinn et al. 2020); the medians (16th and 84th percentiles) of $\log(Z_{*,\text{lw}}/Z_{\odot})$ and $\log(Z_{*,\text{mw}}/Z_{\odot})$ are -0.82 (-0.54 , -1.17) and -0.67 (-0.47 , -0.84), respectively. This points to a decrease in the chemical enrichment with a decrease in the stellar mass of the galaxies. DGs also show a large scatter in stellar metallicities, especially in the mass-weighted one. There is a weak preference for higher metallicities in dwarf ETGs than dwarf LTGs. It is interesting that, on average, $Z_{*,\text{lw}}$ is larger than $Z_{*,\text{mw}}$ for dwarfs (though with a large scatter, including even some galaxies with an inverse result), while for the massive galaxies, $Z_{*,\text{lw}}$ is mostly slightly smaller than $Z_{*,\text{mw}}$. The median (16th and 84th percentiles) of $\log(Z_{*,\text{mw}}/Z_{*,\text{lw}})$ for dwarfs is -0.15 (0.03 , -0.34) dex. The above results suggest that the young stellar populations of most of the dwarfs formed from gas that underwent more chemical enrichment (this probably is reaccreted gas) than the pristine gas from which the old populations formed. In contrast, the opposite is true for massive galaxies; that is, their younger stellar populations were formed from less metallic gas, probably because these systems have accreted significant amounts of mostly pristine gas over their

lifetimes and their old populations were significantly enriched by early SF.

In the middle right panel of Figure 13, we plot several previous measures of $Z_{*,\text{lw}}$ for dwarf and normal galaxies. When necessary, we homogenize to our adopted value of $Z_{\odot} = 0.019$. The solid black line and gray shaded area show the mean relation and its scatter obtained by Kirby et al. (2013) from observations of resolved stars in Local Group dwarfs, both spheroidals and irregulars. The red crosses also correspond to determinations from the spectra of resolved stars—in this case, in local normal galaxies and DGs (Kudritzki et al. 2016, and more references therein). The works of Gallazzi et al. (2005; solid orange line) and Panter et al. (2008; solid red line) used spectral information from the SDSS and applied different analysis techniques and SPS methods for determining $Z_{*,\text{lw}}$. In the case of Zahid et al. (2017; blue crosses), stacked spectra of only SFg were used. In general, the MaNGA $Z_{*,\text{lw}}-M_*$ relation obtained with pyPipe3D is in rough agreement with previous studies. As for the dwarfs, our $Z_{*,\text{lw}}$ determinations are on average higher than those of Kirby et al. (2013) and in good agreement with those of Zahid et al. (2017) and Kudritzki et al. (2016).

In Figure 14, we show the relationship between the $\text{Age}_{\text{mw}}/\text{Age}_{\text{lw}}$ and $Z_{*,\text{mw}}/Z_{*,\text{lw}}$ ratios for the dwarf and whole MaNGA samples. The loci of DGs in this diagram clearly differ from the loci of the most massive galaxies. As discussed

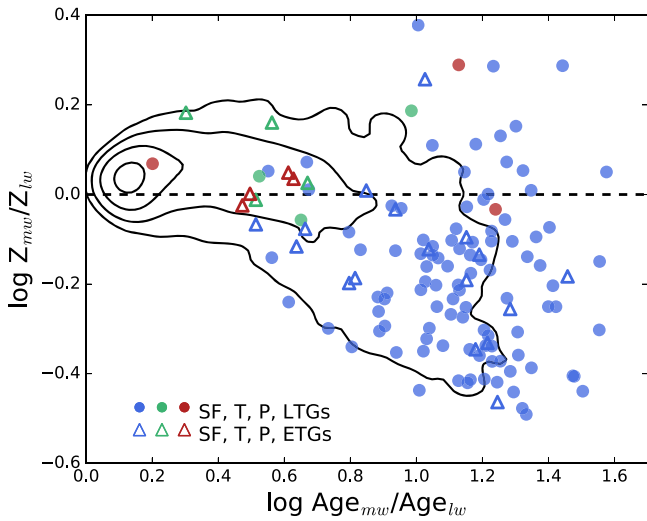


Figure 14. Relationship between the $\text{Age}_{\text{mw}}/\text{Age}_{\text{lw}}$ and $Z_{*,\text{mw}}/Z_{*,\text{lw}}$ ratios shown in the lower panels of Figure 13 for the MaNDala (symbols) and whole MaNGA (isodensity contours) samples. Symbols and colors are as in Figure 13. The isocontours enclose 99%, 96%, 84%, and 37% of the data.

above, for dwarfs, on average, $\text{Age}_{\text{mw}} \gg \text{Age}_{\text{lw}}$ and $Z_{*,\text{mw}} < Z_{*,\text{lw}}$, such that they tend to lie in the lower right side of this diagram, but with a large scatter. The trend seen in Figure 14 suggests a diversity of stellar populations for dwarfs, but in most of the cases they are characterized by a dominant old population with low metallicity and the presence of late, chemically enriched populations. The above points to a diversity of (bursty) SFHs, but characterized, on average, by an intense early phase of transformation of low-metallicity gas into stars and late episodes of SF from chemically enriched gas (the latter suggests a poor or absent contribution of pristine gas accretion during the late evolution of dwarfs). The larger the time interval between early and late bursts of SF episodes, the more enriched is, on average, the gas from which the young populations form.

For massive galaxies, the small values of the $\text{Age}_{\text{mw}}/\text{Age}_{\text{lw}}$ and $Z_{*,\text{mw}}/Z_{*,\text{lw}}$ ratios point to more continuous and homogeneous SFHs, and the fact that $Z_{*,\text{mw}}/Z_{*,\text{lw}}$ tends to be slightly larger than unity suggests that most of the gas out of which form younger stellar populations is of cosmological origin, i.e., it is accreted from the poorly enriched intergalactic medium as the dark matter halo grows. As is well-known, within the Λ CDM cosmogony, the more massive the halos, the later their mass growth occurs (see, e.g., Mo et al. 2010; Rodríguez-Puebla et al. 2016), including the accretion of baryons. Following this trend, the growth of low-mass halos that host DGs is very slow at late epochs. Therefore, most of the gas out of which young populations form in dwarfs galaxies is expected to come from inside the same halo or galaxy; it is (enriched) gas that was likely heated/ejected by early SF in the galaxy that later cools and falls back again. The results presented above agree with this general picture.

Finally, we have explored whether the age- and metallicity-mass relations of our DGs are segregated by being central or satellites or being at distances D_{host} larger or smaller than 1 Mpc. We do not find any clear trend in either case.

5.4.3. Properties of the Global SFH

The SPS analysis of the MaNGA galaxies allows us to reconstruct their full global/local SF, stellar mass, and

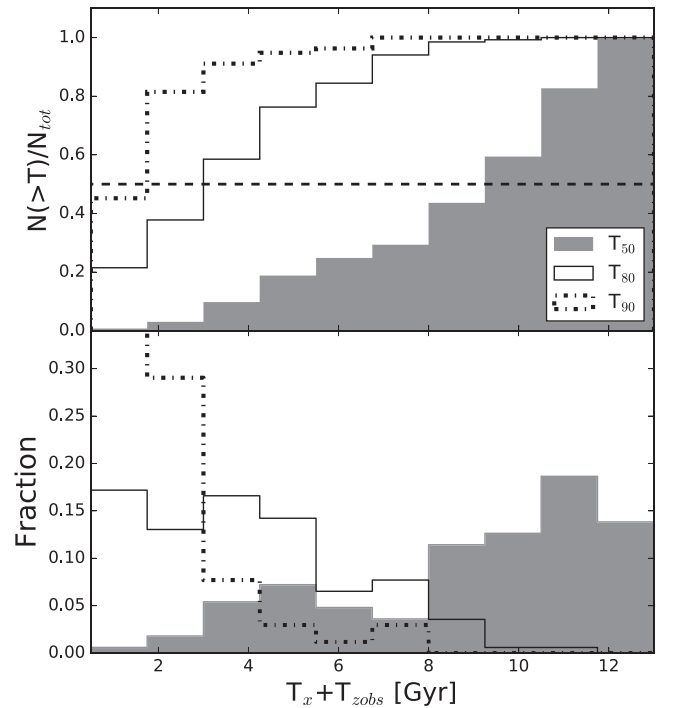


Figure 15. Cumulative (upper panel) and differential (lower panel) distributions of the look-back times at which 50%, 80%, and 90% of the stellar masses of the MaNDala galaxies were formed. T_x , with $x = 50\%$, 80% , and 90% , represents the age at which the given fraction of stars formed, and $T_{z_{\text{obs}}}$ is the look-back time at the observation redshift of a given galaxy for the assumed cosmology in this paper. The dashed line in the upper panel marks the 0.5 value for the cumulative distribution.

chemical enrichment histories (see, e.g., Ibarra-Medel et al. 2016; Goddard et al. 2017; Rowlands et al. 2018; Sánchez et al. 2019; Peterken et al. 2021). In a forthcoming paper, we will present and discuss results related to these histories for the DGs. By using the global stellar mass growth history of each galaxy, we report in the VAC the stellar ages when 50% (T_{50}) and 90% (T_{90}) of the final stellar mass were formed, respectively. Since most of the targets in the MaNDala catalog are at very low redshifts $z < 0.03$ (look-back time less than 0.4 Gyr for the cosmology adopted here), the stellar ages mentioned above differ from the respective cosmic look-back times only by small amounts of time. In any case, we calculate the look-back time at which each galaxy formed a given fraction of its M_* by adding to the respective stellar age (e.g., T_{50}) the look-back time of observation, $T_{z_{\text{obs}}}$. Figure 15 presents the differential and cumulative histograms of the look-back times (for the cosmology adopted here) at which the MaNGA DGs formed 50%, 80%, and 90% of their stellar masses. From the distributions, we see that most of the dwarfs formed half of their stars at very early epochs. For 50% (70%) of them, these epochs correspond to look-back times larger than ≈ 10 (8) Gyr, i.e., $z \gtrsim 1.9$ ($z \gtrsim 1.1$). On the other hand, the formation of the last 20% or 10% of stars in the MaNGA dwarfs happened at late cosmic times. The medians of the look-back times corresponding to 80% and 90% of the formed stars are 3.7 and 1.8 Gyr, respectively, i.e., half of the dwarfs formed the last 20% (10%) of their stars at $z \lesssim 0.33$ ($z \lesssim 0.14$). The above results are in rough agreement with those of Zhou et al. (2020), who also analyzed a sample of MaNGA low-mass galaxies by using a Bayesian spectrum parametric fitting.

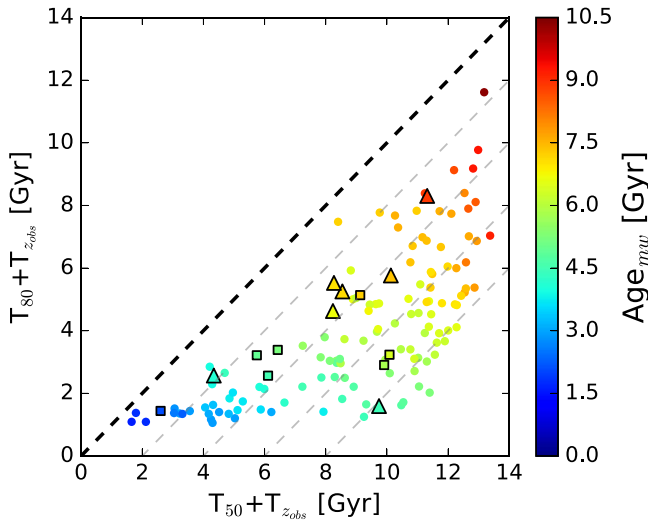


Figure 16. Relationship between the look-back times at which 50% and 80% of the stellar masses of the MaNDala galaxies were formed. The colors of the symbols represent the mass-weighted ages, Age_{mw} . The half-mass look-back time correlates well with Age_{mw} . Circles, squares, and triangles correspond to SFg, T, and P galaxies. The diagonal thin dashed lines indicate differences between the 50% and 80% look-back times of 2, 4, 6, and 8 Gyr.

An interesting question, related to the shape of the SFHs, is how different are the look-back times at which two different stellar mass fractions were formed. In Figure 16, we show the look-back times corresponding to 50% and 80% of the formed stars for the dwarfs. The color indicates the mass-weighted age of each galaxy. First, as expected, there is a good correlation between Age_{mw} and the half-mass formation time, though the former tends to be shorter than the latter by 1–3 Gyr, on average, for ages greater than ~ 4 Gyr. According to Figure 16, the dwarfs that formed 50% of their stars late (≈ 2 –5 Gyr ago or $\text{Age}_{\text{mw}} \approx 1$ –4 Gyr), formed the last 20% of stars very late, i.e., 1–1.5 Gyr ago. For the oldest galaxies, there is a weak trend for the last 20% of stars to form earlier, the earlier the first half of the stars form. The galaxies with higher differences between the formation of the 50% and 80% of their stellar masses (> 6 Gyr) are those with intermediate ages, $\text{Age}_{\text{mw}} \approx 5$ –8 Gyr. The dwarfs classified as passive, P (triangles), present small differences (2–4 Gyr) between the formation of 50% and 80% of their stellar masses. Since these galaxies are retired, they are not expected to have late SF events able to contribute to the late growth of the last 20% of stellar mass.

Finally, in the upper panel of Figure 17, we present the global SFR versus M_* relationship for the MaNDala and the whole MaNGA samples. We have calculated the SFR from the dust-corrected $\text{H}\alpha$ line integrated within the FoV of each galaxy, using the Kennicutt conversion factor corrected to the Chabrier (2003) IMF. In addition, we introduce here a nebular metallicity-dependent correction to this factor. For this, we follow Shin et al. (2021) and use the pyPipe3D nebular metallicity calculated for each MaNDala galaxy. We also apply a correction to our $\text{H}\alpha$ -based SFR, which for dwarfs is systematically underpredicted with respect to the FUV-based SFR (Lee et al. 2009). This is likely because, at low SFRs, statistically sampling the IMF does not produce enough massive OB stars, resulting in a deficit for $\text{H}\alpha$ measurements (Weidner et al. 2013). This correction is applied following Shin et al. (2021), and it is actually very small for most of our dwarfs.

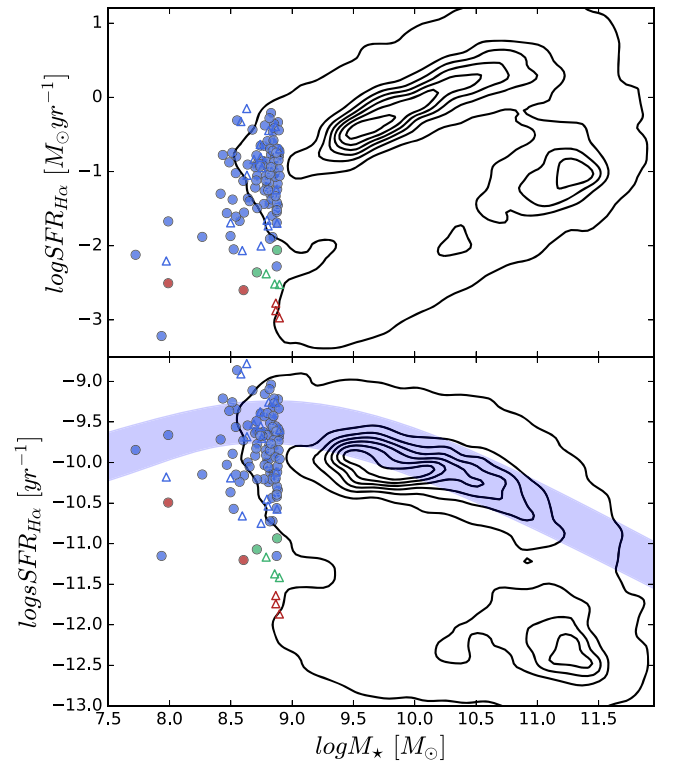


Figure 17. Upper panel: Global SFR vs. M_* for the MaNDala (circles) and whole MaNGA (isodensity contours) samples. The SFRs were calculated from the $\text{H}\alpha$ line integrated within the FoV of each galaxy using the Chabrier IMF (see text). The stellar masses are from the NSA catalog. No correction for volume completeness was applied. Lower panel: Same as in the upper panel but for the specific SFR. The shaded area is the 1σ region describing the SF main sequence inferred from several observational data at $z \sim 0.1$ by Rodríguez-Puebla et al. (2020a).

Dwarf SFgs (blue circles) follow roughly the trend toward low masses of the main sequence of galaxies of the whole sample, though with a large scatter. The few dwarfs classified as P and T (red and green colors, respectively), as expected, lie far below the SF main sequence. The lower panel of Figure 17 shows the sSFR ($=\text{SFR}/M_*$) versus M_* . The data at lower masses are scarce but they hint at a *bending in the specific SFR – M_* relation at masses around $10^9 M_\odot$* , in accordance with some previous observations and empirical inferences (e.g., Skibba et al. 2011; McGaugh et al. 2017; Rodríguez-Puebla et al. 2020a). The local SF main sequence inferred by the latter authors from a large set of observations from the FUV to the FIR (obeying volume completeness) is overplotted in the lower panel of Figure 17. Despite the large differences in the methodologies, and taking into account that the isocontours plotted in Figure 17 are not corrected by volume completeness, the agreement here is reasonable, including its extension to dwarfs.

6. Summary and Discussion

In this work, we present the sample of DGs observed by the project MaNGA, for which we perform photometric and spectroscopic analyses using DESI and MaNGA data, respectively. The sample is conformed by 136 galaxies that were selected to have $M_* < 10^{9.06} M_\odot$ and $M_g > -18.5$,²⁸ and it is to our knowledge the first large sample of DGs observed with IFS data.

²⁸ According to the stellar masses and absolute magnitudes from the NSA Catalog.

The photometric analyses, carried out in the g , r , and z bands, provide SB profiles that were fitted with a Sérsic function convolved with a Moffat function to describe the PSF of the photometric measurements. Due to the depth of the DESI images, the fitted SB profiles extend, on average, to ~ 6 , 4.5, and $3.5 R_e$ in the g , r , and z bands, respectively. Along with these, other radial profiles such as P.A., ϵ , and color are obtained. The main results of this analysis are summarized as follows:

1. The galaxies comprising our sample, called MaNDala, are mainly bright dwarfs; this is particularly evident when compared with other DG samples, such as the one presented by Poulain et al. (2021). The mean stellar mass of the sample is $10^{8.89} M_\odot$, while the mean absolute magnitude in g is -16.92 mag. The sample is dominated by late-type and central galaxies.
2. The Sérsic index and the central and effective SBs of the dwarf ETGs tend to be higher and have a greater dispersion than those of the dwarf LTGs. In general, the former are more compact and redder than the latter. Most MaNDala galaxies have nearly flat color profiles.
3. The location of our galaxies within the $R_e - M_g$, $\langle \mu_{e,g} \rangle - M_g$, and $\langle \mu_{e,g} \rangle - R_e$ (Kormendy) diagrams shows that this sample has a very large scatter in the implied relations. This makes visible the variety of MaNDala galaxies, which can range from very low SB and extended (UDG candidates) to high SB and compact.
4. Late- and early-type DGs occupy roughly the same regions in the Kormendy diagrams, with a slight preference of the former to be more extended and of lower SB than the latter.
5. MaNDala galaxies show a large scatter in the magnitude– or mass–size relations, consistent with NSA DGs or other DG samples, and confirm flattening in the $-19 \leq M_g < -15$ or $10^8 \leq (M_*/M_\odot) < 10^9$ ranges of these relations with respect to the more luminous/massive galaxies.

The spectroscopic analysis, performed in apertures containing the entire MaNGA FoV, made use of a nonparametric SPS analysis in spatial bins of $S/N > 50$ (pyPipe3D code). A single-component Gaussian fit to the emission lines was performed afterward. The main results from this analysis are summarized as follows:

1. Using emission line criteria, the dwarfs were classified into star-forming (92%), transitioning (4%), and passive (4%) galaxies; no conclusive signatures of nuclear activity were found in any of them. The vast majority of dwarf LTGs, 96%, are SFg; even dwarf ETGs are mostly SFg, 75%.
2. The 16th–84th percentiles of Age_{mw} and Age_{lw} are 7.1–4.2 Gyr and 0.6–0.3 Gyr, respectively. The Age_{mw} values of dwarfs are, on average, slightly smaller than those of massive galaxies, while these differences are much larger in the case of Age_{lw} . As for the stellar metallicities of our dwarfs, they are much lower than those of massive galaxies, and present a large scatter; the 16th–84th percentiles of $\log(Z_{*,\text{mw}}/Z_\odot)$ and $\log(Z_{*,\text{lw}}/Z_\odot)$ are $(-0.54, -1.17)$ and $(-0.47, -0.84)$, respectively.
3. The loci of dwarfs in the $\text{Age}_{\text{mw}}/\text{Age}_{\text{lw}}$ versus $Z_{*,\text{mw}}/Z_{*,\text{lw}}$ plane are different from massive galaxies. For dwarfs, on average, $\text{Age}_{\text{mw}} \gg \text{Age}_{\text{lw}}$ and $Z_{*,\text{mw}} < Z_{*,\text{lw}}$ (with a large scatter), with a trend of a lower $Z_{*,\text{mw}}/Z_{*,\text{lw}}$ ratio as $\text{Age}_{\text{mw}}/\text{Age}_{\text{lw}}$ increases. The above evidence points to a diversity of SFHs, but characterized, on

average, by an intense early phase of transformation of low-metallicity gas into stars and late episodes of SF from chemically enriched gas. The greater the time interval between the early burst and the final episodes of SF, the more enriched, on average, is the gas from which young populations are formed.

4. Half of the dwarfs formed 50% of their stellar mass at early epochs, $z \gtrsim 2$. However, the formation of the last 20% of the mass happened recently ($\lesssim 0.3$ for half of the sample). The T and P dwarfs are those with less differences in their epochs of 50% and 80% stellar mass formation (~ 2 –4 Gyr), while SFg dwarfs with intermediate ages show differences larger than 6 Gyr, that is, their SFHs tend to have an early period of intense SF and very late SF episodes.
5. The H_α -based SFRs of our dwarfs present a large scatter. In the $s\text{SFR}-M_*$ diagram, the SFg dwarfs seem to follow the SF main sequence of the more massive galaxies, but showing evidence of a bending of this relation at $M_* \sim 10^9 M_\odot$, with a median maximum value of $\log(s\text{SFR}/M_\odot \text{ yr}^{-1}) \approx -9.7$.

It should be said that we did not find significant differences between the central and satellite dwarfs, nor between the isolated and grouped dwarfs in any of the photometric/structural or stellar population relations presented here. The above may imply that the internal processes in the presence of a low gravitational potential are more relevant in shaping the properties of dwarfs than the external processes associated to the environment (e.g., Dunn 2015, but see, e.g., Weisz et al. 2011; Young et al. 2014).

Using new public data from deep photometric instruments, such as the data set provided by the DESI collaboration, offers the advantage of making more precise inferences, not only regarding the global characteristics of galaxies but also the true shape of the SB and geometric profiles of galaxies up to fainter SB values and to large radii, than the SDSS photometric instrument is able to provide. This may have an impact when investigating in detail the structure of these objects, but also when seeking to restrict kinematical analyses that require the use of precise geometrical parameters.

On the other hand, the use of IFS observations, such as the ones MaNGA provides, allows us to access spatially resolved spectroscopic observations, which give homogeneous information about their stellar and ionized gaseous components. In the near future, we aim to extend our analysis to fully exploit the resolved nature of this data set, extending the integrated results presented here.

Authors wish to acknowledge the comments given by the anonymous referee, which were very helpful to improve this work. Authors wish to acknowledge Claudia Castro Rodríguez, for her help generating a fraction of the mosaic images for the MaNDala SDSS-IV VAC, and for designing and developing the project web page. M.C.D. acknowledges support from CONACYT "Ciencia de Frontera" grant 320199.

M.C.D. and H.M.H.T. acknowledge support from UC MEXUS-CONACYT grant CN-17-128. A.R.P. acknowledges support from the CONACyT "Ciencia Basica" grant 285721. E.A.O. acknowledges support from the SECTEI (Secretaría de Educación, Ciencia, Tecnología e Innovación de la Ciudad de México) under the Postdoctoral Fellowship SECTEI/170/2021 and CM-SECTEI/303/2021.

Funding for the Sloan Digital Sky Survey IV has been provided by the Alfred P. Sloan Foundation, the U.S. Department of Energy Office of Science, and the Participating Institutions.

SDSS-IV acknowledges support and resources from the Center for High Performance Computing at the University of Utah. The SDSS website is www.sdss.org.

SDSS-IV is managed by the Astrophysical Research Consortium for the Participating Institutions of the SDSS Collaboration, including the Brazilian Participation Group, the Carnegie Institution for Science, Carnegie Mellon University, Center for Astrophysics | Harvard & Smithsonian, the Chilean Participation Group, the French Participation Group, Instituto de Astrofísica de Canarias, The Johns Hopkins University, Kavli Institute for the Physics and Mathematics of the Universe (IPMU)/University of Tokyo, the Korean Participation Group, Lawrence Berkeley National Laboratory, Leibniz Institut für Astrophysik Potsdam (AIP), Max-Planck-Institut für Astronomie (MPIA Heidelberg), Max-Planck-Institut für Astrophysik (MPA Garching), Max-Planck-Institut für Extraterrestrische Physik (MPE), National Astronomical Observatories of China, New Mexico State University, New York University, University of Notre Dame, Observatório Nacional/MCTI, The Ohio State University, Pennsylvania State University, Shanghai Astronomical Observatory, United Kingdom Participation Group, Universidad Nacional Autónoma de México, University of Arizona, University of Colorado Boulder, University of Oxford, University of Portsmouth, University of Utah,

University of Virginia, University of Washington, University of Wisconsin, Vanderbilt University, and Yale University.

This project makes use of the MaNGA-Pipe3D data products. The data products used in this project benefited from the computational and human resources provided by the LAMOD- UNAM project through the clusters Atocatl and Tochtli. LAMOD is a collaborative effort between the IA, ICN, and IQ institutes at UNAM and DGAPA UNAM grants PAPIIT IG101620 and IG10122. We thank the IA-UNAM MaNGA team for creating this catalog, and the CONACyT-180125 project for supporting them.

Appendix The SDSS-IV MaNDala Value Added Catalog

All results presented in this work are available for public use as a Value Added Catalog (VAC) for the SDSS-IV Consortium named MaNDala. These results make up the first version of the MaNDala VAC (V1.0), and correspond to 136 galaxies of our sample. This version is being released as part of the SDSS DR17. A second version of this catalog is expected to be released in the future, and will be available from the same URLs given in this paper.

The data can be retrieved as a single Flexible Image Transport System²⁹ (FITS) format table named `mandala_v1_0.fits`, through the SDSS public repository.³⁰ In addition, a collection of mosaic images in PDF format, like the one presented in Figure 2, are also available through the same site.

Table 2
Data Model of the MaNDala VAC FITS Format Table

Column No.	Name	Type	Units	Description
1	Plateifu	String		MaNGA Plate-IFU
2	MangaID	String		MaNGA ID
3	R.A.	Float	deg	NSA R.A. (J200)
4	Dec	Float	deg	NSA decl. (J2000)
5	IAUName	String		IAU Name
6	NSA_ID	Integer		NSA ID
7	NSA_redshift	Float		NSA Redshift
8	NSA_LogSérsicMass	Float	$h^{-2} M_{\odot}$	Logarithm of NSA Sérsic Mass
9	Radius	Float Array	arcsec	DESI Profiles Radii
10	SB_g	Float Array	mag arcsec ⁻²	g-band DESI Surface Brightness Profiles
11	SB_g_err	Float Array	mag arcsec ⁻²	g-band DESI Surface Brightness Profiles Errors
12	SB_r	Float Array	mag arcsec ⁻²	r-band DESI Surface Brightness Profiles
13	SB_r_err	Float Array	mag arcsec ⁻²	r-band DESI Surface Brightness Profiles Errors
14	SB_z	Float Array	mag arcsec ⁻²	z-band DESI Surface Brightness Profiles
15	SB_z_err	Float Array	mag arcsec ⁻²	z-band DESI Surface Brightness Profiles Errors
16	P.A_r	Float Array	degrees	r-band DESI Position Angle Profiles
17	P.A_r_err	Float Array	degrees	r-band DESI Position Angle Profiles Errors
18	Ellipticity_r	Float Array		r-band DESI Ellipticity Profiles
19	Ellipticity_r_err	Float Array		r-band DESI Ellipticity Profiles Errors
20	Flux_r	Float Array	nanomaggies	r-band DESI Accumulated Flux Profile
21	Interpolated_Reff_r	Float	arcsec	r-band R_e Derived from the Accumulated Flux
22	Interpolated_R90_r	Float	arcsec	r-band Radius at 90% of Light Derived from the Accumulated Flux
23	Ellip_R90_r	Float		r-band Ellipticity at Radius at 90% of Light
24	P.A_R90_r	Float	degrees	r-band P.A. at Radius at 90% of Light
25	Sérsic_SB_eff_g	Float	mag arcsec ⁻²	g-band Sérsic Surface Brightness at R_e
26	Sérsic_SB_eff_g_err	Float	mag arcsec ⁻²	g-band Sérsic Surface Brightness at R_e Error
27	Sérsic_Reff_g	Float	arcsec	g-band Sérsic R_e
28	Sérsic_Reff_g_err	Float	arcsec	g-band Sérsic R_e Error
29	n_Sérsic_g	Float		g-band n Sérsic Index

²⁹ https://fits.gsfc.nasa.gov/fits_documentation.html

³⁰ <https://data.sdss.org/sas/dr17/manga/mandala>

Table 2
(Continued)








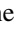
Column No.	Name	Type	Units	Description
30	n_Sérsic_g_err	Float		g-band n Sérsic Index Error
31	Sérsic_SB_0_g	Float	mag arcsec ⁻²	g-band Sérsic Central Surface Brightness
32	Sérsic_AppMag_g	Float	mag	g-band Sérsic Apparent Magnitude
33	Sérsic_AbsMag_g	Float	mag	g-band Sérsic Absolute Magnitude (h = 1)
34	Sérsic_Chi2_g	Float		g-band Reduced Chi ² for Sérsic fit
35	Sérsic_SB_eff_r	Float	mag arcsec ⁻²	r-band Sérsic Surface Brightness at R_e
36	Sérsic_SB_eff_r_err	Float	mag arcsec ⁻²	r-band Sérsic Surface Brightness at R_e Error
37	Sérsic_Reff_r	Float	arcsec	r-band Sérsic R_e
38	Sérsic_Reff_r_err	Float	arcsec	r-band Sérsic R_e Error
39	n_Sérsic_r	Float		r-band n Sérsic Index
40	n_Sérsic_r_err	Float		r-band n Sérsic Index Error
41	Sérsic_SB_0_r	Float	mag arcsec ⁻²	r-band Sérsic Central Surface Brightness
42	Sérsic_AppMag_r	Float	mag	r-band Sérsic Apparent Magnitude
43	Sérsic_AbsMag_r	Float	mag	r-band Sérsic Absolute Magnitude (h = 1)
44	Sérsic_Chi2_r	Float		r-band Reduced Chi ² for Sérsic fit
45	Sérsic_SB_eff_z	Float	mag arcsec ⁻²	z-band Sérsic Surface Brightness at R_e
46	Sérsic_SB_eff_z_err	Float	mag arcsec ⁻²	z-band Sérsic Surface Brightness at R_e Error
47	Sérsic_Reff_z	Float	arcsec	z-band Sérsic R_e
48	Sérsic_Reff_z_err	Float	arcsec	z-band Sérsic R_e Error
49	n_Sérsic_z	Float		z-band n Sérsic Index
50	n_Sérsic_z_err	Float		z-band n Sérsic Index Error
51	Sérsic_SB_0_z	Float	mag arcsec ⁻²	z-band Sérsic Central Surface Brightness
52	Sérsic_AppMag_z	Float	mag	z-band Sérsic Apparent Magnitude
53	Sérsic_AbsMag_z	Float	mag	z-band Sérsic Absolute Magnitude (h = 1)
54	Sérsic_Chi2_z	Float		z-band Reduced Chi ² for Sérsic Fit
55	Stellar_mass_FoV	Float	M_{\odot}	Log Stellar Mass within the FoV ^a
56	Stellar_mass_Reff	Float	M_{\odot}	Log Stellar Mass within $1 R_e^b$
57	SFRssp_FoV	Float	$M_{\odot} \text{ yr}^{-1}$	Log SSP Star Formation Rate within the FoV ^a
58	SFRssp_Reff	Float	$M_{\odot} \text{ yr}^{-1}$	Log SSP Star Formation Rate within $1 R_e^b$
59	T50_FoV	Float	yr	Log formation Time When the Galaxy Reached 50% of Its Total Stellar Mass (Calculated within the FoV ^a)
60	T50_Re	Float	yr	Log formation Time When the Galaxy Reached 50% of Its Total Stellar Mass (Calculated within $1 R_e^b$)
61	T90_FoV	Float	yr	Log formation Time When the Galaxy Reached 90% of Its Total Stellar Mass (Calculated within the FoV ^a)
62	T90_Re	Float	yr	Log formation Time When the Galaxy Reached 90% of Its Total Stellar Mass (Calculated within $1 R_e^b$)
63	D4000_FoV	Float	dex	Average D4000 Value Defined within the FoV ^a
64	D4000_Reff	Float	dex	Average D4000 Value Defined within $1 R_e^b$
65	Age_lum_FoV	Float	yr	Average Log Luminosity-weighted Age within the FoV ^a
66	Age_lum_Reff	Float	yr	Average Log Luminosity-weighted Age within $1 R_e^b$
67	Age_mass_FoV	Float	yr	Average Log Mass-weighted Age within the FoV ^a
68	Age_mass_Reff	Float	yr	Average Log Mass-weighted Age within the R_e^b
69	Metallicity_lum_FoV	Float	ZH	Average Log Luminosity-weighted Metallicity within the FoV ^a
70	Metallicity_lum_Reff	Float	ZH	Average Log Luminosity-weighted Metallicity within $1 R_e^b$
71	Metallicity_mass_FoV	Float	ZH	Average Log Mass-weighted Metallicity within the FoV ^a
72	Metallicity_mass_Reff	Float	ZH	Average Log Mass-weighted Metallicity within $1 R_e^b$
73	SFRHa_FoV	Float	$M_{\odot} \text{ yr}^{-1}$	Log H α Star Formation Rate within the FoV ^a
74	SFRHa_Reff	Float	$M_{\odot} \text{ yr}^{-1}$	Log H α Star Formation Rate within $1 R_e^b$
75	Ha_FoV	Float	erg s ⁻¹ cm ⁻²	Log H α flux within the FoV ^a
76	Ha_Reff	Float	erg s ⁻¹ cm ⁻²	Log H α flux within $1 R_e^a$
77	Hb_FoV	Float	erg s ⁻¹ cm ⁻²	Log H β flux within the FoV ^a
78	Hb_Reff	Float	erg s ⁻¹ cm ⁻²	Log H β flux within $1 R_e^b$
79	N II_FoV	Float	erg s ⁻¹ cm ⁻²	Log [N II] ₆₅₈₃ flux within the FoV ^a
80	N II_Reff	Float	erg s ⁻¹ cm ⁻²	Log [N II] ₆₅₈₃ flux within $1 R_e^b$
81	O III_FoV	Float	erg s ⁻¹ cm ⁻²	Log [O III] ₅₀₀₇ flux within the FoV ^a
82	O III_Reff	Float	erg s ⁻¹ cm ⁻²	Log [O III] ₅₀₀₇ flux within $1 R_e^b$
83	EWHa_FoV	Float		Equivalent Width of H α within the FoV ^a
84	EWHa_Reff	Float		Equivalent Width of H α within $1 R_e^b$

Notes.^a Quantities given within the Field of View (FoV) are calculated within the MaNGA FoV.^b Quantities given within one effective radius (Reff) are calculated using our estimation of the R_e from the Sérsic fit (column 37).

The documentation of the MaNDala VAC is available through the SDSS Value Added Catalogs web page.³¹ Details of the MaNDala VAC FITS format file, coined the data model, are given in Table 2. The same data model can also be found on the SDSS web page for this catalog,³² and on our own site for this project,³³ from which the reader may find extra information about the MaNDala project.

The file `mandala_v1_0.fits` consist of two extensions, a header (HDU0) containing information about the data products from DESI and MaNGA used to derive our results, and the principal extension (HDU1), in which the results are stored in the form of a 84 columns table. Columns 1 to 54 in the MaNDala VAC FITS table contain the photometric results derived with the DESI data (see Section 2.1), which are described in Sections 4.1, 4.2, 4.2.1, and 5.3. Columns 55 to 84 contain spectroscopic results derived with MaNGA data (see Section 2.2), which are described in Sections 4.3 and 5.4.

ORCID iDs

M. Cano-Díaz  <https://orcid.org/0000-0001-9553-8230>
 H. M. Hernández-Toledo  <https://orcid.org/0000-0001-9601-7779>
 A. Rodríguez-Puebla  <https://orcid.org/0000-0002-0170-5358>
 H. J. Ibarra-Medel  <https://orcid.org/0000-0002-9790-6313>
 V. Ávila-Reese  <https://orcid.org/0000-0002-3461-2342>
 O. Valenzuela  <https://orcid.org/0000-0002-0523-5509>
 A. E. Medellin-Hurtado  <https://orcid.org/0000-0002-7805-6982>
 J. A. Vázquez-Mata  <https://orcid.org/0000-0001-8694-1204>
 A. Weijmans  <https://orcid.org/0000-0002-5908-6852>
 J. J. González  <https://orcid.org/0000-0002-3724-1583>
 E. Aquino-Ortiz  <https://orcid.org/0000-0003-1083-9208>
 L. A. Martínez-Vázquez  <https://orcid.org/0000-0001-7608-5360>
 Richard R. Lane  <https://orcid.org/0000-0003-1805-0316>

References

- Abazajian, K. N., Adelman-McCarthy, J. K., Agüeros, M. A., et al. 2009, *ApJS*, 182, 543
- Abdurro'uf, Accetta, K., Aerts, C., et al. 2021, *ApJS*, 259, 35
- Ann, H. B., Seo, M., & Ha, D. K. 2015, *ApJS*, 217, 27
- Aquino-Ortiz, E., Sánchez, S. F., Valenzuela, O., et al. 2020, *ApJ*, 900, 109
- Arora, N., Stone, C., Courteau, S., & Jarrett, T. H. 2021, *MNRAS*, 505, 3135
- Avila-Reese, V., & Firmani, C. 2011, *RMxAA*, 40, 27
- Baldwin, J. A., Phillips, M. M., & Terlevich, R. 1981, *PASP*, 93, 5
- Bennet, P., Sand, D. J., Crnojević, D., et al. 2017, *ApJ*, 850, 109
- Blanton, M. R., Kazin, E., Muna, D., Weaver, B. A., & Price-Whelan, A. 2011, *AJ*, 142, 31
- Blanton, M. R., & Moustakas, J. 2009, *ARA&A*, 47, 159
- Blanton, M. R., Bershady, M. A., Abolfathi, B., et al. 2017, *AJ*, 154, 28
- Bullock, J. S., & Boylan-Kolchin, M. 2017, *ARA&A*, 55, 343
- Bundy, K., Bershady, M. A., Law, D. R., et al. 2015, *ApJ*, 798, 7
- Cano-Díaz, M., Ávila-Reese, V., Sánchez, S. F., et al. 2019, *MNRAS*, 488, 3929
- Cano-Díaz, M., Sánchez, S. F., Zibetti, S., et al. 2016, *ApJL*, 821, L26
- Cardelli, J. A., Clayton, G. C., & Mathis, J. S. 1989, *ApJ*, 345, 245
- Carlsten, S. G., Greco, J. P., Beaton, R. L., & Greene, J. E. 2020, *ApJ*, 891, 144
- Carlsten, S. G., Greene, J. E., Greco, J. P., Beaton, R. L., & Kado-Fong, E. 2021, *ApJ*, 922, 267
- Catalán-Torrecilla, C., Gil de Paz, A., Castillo-Morales, A., et al. 2017, *ApJ*, 848, 87
- Chabrier, G. 2003, *PASP*, 115, 763
- Ciotti, L., & Bertin, G. 1999, *A&A*, 352, 447
- Colin, P., Avila-Reese, V., González-Samaniego, A., & Velázquez, H. 2015, *ApJ*, 803, 28
- Crnojević, D., Sand, D. J., Spekkens, K., et al. 2016, *ApJ*, 823, 19
- Dalcanton, J. J., Williams, B. F., Seth, A. C., et al. 2009, *ApJS*, 183, 67
- De Lucia, G. 2019, *Galax*, 7, 56
- DESI Collaboration, Aghamousa, A., Aguilar, J., et al. 2016, arXiv:1611.00037
- Dey, A., Schlegel, D. J., Lang, D., et al. 2019, *AJ*, 157, 168
- Dragomir, R., Rodríguez-Puebla, A., Primack, J. R., & Lee, C. T. 2018, *MNRAS*, 476, 741
- Drory, N., MacDonald, N., Bershady, M. A., et al. 2015, *AJ*, 149, 77
- Dunn, J. M. 2015, *MNRAS*, 453, 1799
- Eigenthaler, P., Puzia, T. H., Taylor, M. A., et al. 2018, *ApJ*, 855, 142
- Ferrarese, L., Côté, P., Cuillandre, J.-C., et al. 2012, *ApJS*, 200, 4
- Ferrarese, L., Côté, P., MacArthur, L. A., et al. 2020, *ApJ*, 890, 128
- Flaugher, B., Diehl, H. T., Honscheid, K., et al. 2015, *AJ*, 150, 150
- Gallazzi, A., Charlot, S., Brinchmann, J., White, S. D. M., & Tremonti, C. A. 2005, *MNRAS*, 362, 41
- Garma-Oehmichen, L., Cano-Díaz, M., Hernández-Toledo, H., et al. 2020, *MNRAS*, 491, 3655
- Ge, J., Mao, S., Lu, Y., et al. 2021, *MNRAS*, 507, 2488
- Geha, M., Blanton, M. R., Yan, R., & Tinker, J. L. 2012, *ApJ*, 757, 85
- Goddard, D., Thomas, D., Maraston, C., et al. 2017, *MNRAS*, 466, 4731
- Graham, A. W., & Driver, S. P. 2005, *PASA*, 22, 118
- Gunn, J. E., Siegmund, W. A., Mannery, E. J., et al. 2006, *AJ*, 131, 2332
- Habas, R., Marleau, F. R., Duc, P.-A., et al. 2020, *MNRAS*, 491, 1901
- Hidalgo, S. L. 2017, *A&A*, 606, A115
- Ho, I. T., Medling, A. M., Bland-Hawthorn, J., et al. 2016, *MNRAS*, 457, 1257
- Huertas-Company, M., Aguerri, J. A. L., Bernardi, M., Mei, S., & Sánchez Almeida, J. 2011, *A&A*, 525, A157
- Hunter, D. A., Ficut-Vicas, D., Ashley, T., et al. 2012, *AJ*, 144, 134
- Ibarra-Medel, H. J., Sánchez, S. F., Avila-Reese, V., et al. 2016, *MNRAS*, 463, 2799
- Ikuta, C., & Arimoto, N. 2002, *A&A*, 391, 55
- Jedrzejewski, R. I. 1987, *MNRAS*, 226, 747
- Karachentsev, I. D., Makarov, D. I., & Kaisina, E. I. 2013, *AJ*, 145, 101
- Kauffmann, G., Heckman, T. M., White, S. D. M., et al. 2003, *MNRAS*, 341, 33
- Kewley, L. J., Dopita, M. A., Sutherland, R. S., Heisler, C. A., & Trevena, J. 2001, *ApJ*, 556, 121
- Kim, S., Rey, S.-C., Jerjen, H., et al. 2014, *ApJS*, 215, 22
- Kirby, E. N., Cohen, J. G., Guhathakurta, P., et al. 2013, *ApJ*, 779, 102
- Kormendy, J. 1977, *ApJ*, 218, 333
- Kormendy, J. 1985, *ApJ*, 295, 73
- Kudritzki, R. P., Castro, N., Urbaneja, M. A., et al. 2016, *ApJ*, 829, 70
- Lacerda, E. A. D., Sánchez, S. F., Mejía-Narváez, A., et al. 2022, *NewA*, 97, 101895
- Lacerna, I., Ibarra-Medel, H., Avila-Reese, V., et al. 2020, *A&A*, 644, A117
- Lange, R., Driver, S. P., Robotham, A. S. G., et al. 2015, *MNRAS*, 447, 2603
- Law, D. R., Yan, R., Bershady, M. A., et al. 2015, *AJ*, 150, 19
- Law, D. R., Cherinka, B., Yan, R., et al. 2016, *AJ*, 152, 83
- Lee, J. C., Gil de Paz, A., Tremonti, C., et al. 2009, *ApJ*, 706, 599
- Leitner, S. N. 2012, *ApJ*, 745, 149
- Lim, S., Côté, P., Peng, E. W., et al. 2020, *ApJ*, 899, 69
- Mao, Y.-Y., Geha, M., Wechsler, R. H., et al. 2021, *ApJ*, 907, 85
- McConnachie, A. W. 2012, *AJ*, 144, 4
- McGaugh, S. S., Schombert, J. M., & Lelli, F. 2017, *ApJ*, 851, 22
- McQuinn, K. B. W., Berg, D. A., Skillman, E. D., et al. 2020, *ApJ*, 891, 181
- Meert, A., Vikram, V., & Bernardi, M. 2013, *MNRAS*, 433, 1344
- Meert, A., Vikram, V., & Bernardi, M. 2016, *MNRAS*, 455, 2440
- Mezcua, M., & Domínguez Sánchez, H. 2020, *ApJL*, 898, L30
- Mingozzi, M., Cresci, G., Venturi, G., et al. 2019, *A&A*, 622, A146
- Mo, H., van den Bosch, F. C., & White, S. 2010, *Galaxy Formation and Evolution* (Cambridge: Cambridge Univ. Press)
- Moffat, A. F. J. 1969, *A&A*, 3, 455
- Nedkova, K. V., Häußler, B., Marchesini, D., et al. 2021, *MNRAS*, 506, 928
- Neumann, J., Fragkoudi, F., Pérez, I., et al. 2020, *A&A*, 637, A56
- Ott, J., Stülp, A. M., Warren, S. R., et al. 2012, *AJ*, 144, 123
- Panther, B., Jimenez, R., Heavens, A. F., & Charlot, S. 2008, *MNRAS*, 391, 1117
- Penny, S. J., Masters, K. L., Smethurst, R., et al. 2018, *MNRAS*, 476, 979
- Pérez, E., Cid Fernandes, R., González Delgado, R. M., et al. 2013, *ApJL*, 764, L1
- Peterken, T., Aragón-Salamanca, A., Merrifield, M., et al. 2021, *MNRAS*, 502, 3128

³¹ https://www.sdss.org/dr17/data_access/value-added-catalogs/

³² https://data.sdss.org/datamodel/files/MANGA_MANDALA

³³ <https://mandalasample.wordpress.com>

- Plauchu-Frayn, I., Del Olmo, A., Coziol, R., & Torres-Papaqui, J. P. 2012, *A&A*, **546**, A48
- Poulain, M., Marleau, F. R., Habas, R., et al. 2021, *MNRAS*, **506**, 5494
- Raouf, M., Smith, R., Khosroshahi, H. G., et al. 2021, *ApJ*, **908**, 123
- Rodríguez-Puebla, A., Avila-Reese, V., Cano-Díaz, M., et al. 2020a, *ApJ*, **905**, 171
- Rodríguez-Puebla, A., Avila-Reese, V., & Drory, N. 2013, *ApJ*, **767**, 92
- Rodríguez-Puebla, A., Behroozi, P., Primack, J., et al. 2016, *MNRAS*, **462**, 893
- Rodríguez-Puebla, A., Calette, A. R., Avila-Reese, V., Rodríguez-Gomez, V., & Huertas-Company, M. 2020b, *PASA*, **37**, e024
- Rowlands, K., Heckman, T., Wild, V., et al. 2018, *MNRAS*, **480**, 2544
- Salpeter, E. E. 1955, *ApJ*, **121**, 161
- Sánchez, S. F., Barrera-Ballesteros, J. K., Lacerda, E., et al. 2022, arXiv:2206.07062
- Sánchez, S. F. 2020, *ARA&A*, **58**, 99
- Sánchez, S. F., Rosales-Ortega, F. F., Iglesias-Páramo, J., et al. 2014, *A&A*, **563**, A49
- Sánchez, S. F., Pérez, E., Sánchez-Blázquez, P., et al. 2016a, *RMxAA*, **52**, 21
- Sánchez, S. F., Pérez, E., Sánchez-Blázquez, P., et al. 2016b, *RMxAA*, **52**, 171
- Sánchez, S. F., Avila-Reese, V., Hernandez-Toledo, H., et al. 2018, *RMxAA*, **54**, 217
- Sánchez, S. F., Avila-Reese, V., Rodríguez-Puebla, A., et al. 2019, *MNRAS*, **482**, 1557
- Schaefer, A. L., Croom, S. M., Scott, N., et al. 2019, *MNRAS*, **483**, 2851
- Sérsic, J. L. 1963, *BAAA*, **6**, 41
- Shin, K., Ly, C., Malkan, M. A., et al. 2021, *MNRAS*, **501**, 2231
- Skibba, R. A., Engelbracht, C. W., Dale, D., et al. 2011, *ApJ*, **738**, 89
- Smee, S. A., Gunn, J. E., Uomoto, A., et al. 2013, *AJ*, **146**, 32
- Somerville, R. S., & Davé, R. 2015, *ARA&A*, **53**, 51
- Stierwalt, S., Besla, G., Patton, D., et al. 2015, *ApJ*, **805**, 2
- Stierwalt, S., Liss, S. E., Johnson, K. E., et al. 2017, *NatAs*, **1**, 0025
- Strauss, M. A., Weinberg, D. H., Lupton, R. H., et al. 2002, *AJ*, **124**, 1810
- Tanoglidis, D., Drlica-Wagner, A., Wei, K., et al. 2021, *ApJS*, **252**, 18
- Tolstoy, E., Hill, V., & Tosi, M. 2009, *ARA&A*, **47**, 371
- Trujillo, I., Aguerri, J. A. L., Cepa, J., & Gutiérrez, C. M. 2001, *MNRAS*, **328**, 977
- van Dokkum, P. G., Abraham, R., Merritt, A., et al. 2015, *ApJL*, **798**, L45
- Vázquez-Mata, J. A., Hernández-Toledo, H. M., Avila-Reese, V., et al. 2022, *MNRAS*, **512**, 2222
- Veilleux, S., & Osterbrock, D. E. 1987, *ApJS*, **63**, 295
- Venhola, A., Peletier, R., Laurikainen, E., et al. 2019, *A&A*, **625**, A143
- Wake, D. A., Bundy, K., Diamond-Stanic, A. M., et al. 2017, *AJ*, **154**, 86
- Weidner, C., Kroupa, P., Pflamm-Altenburg, J., & Vazdekis, A. 2013, *MNRAS*, **436**, 3309
- Weinberg, D. H., Bullock, J. S., Governato, F., Kuzio de Naray, R., & Peter, A. H. G. 2015, *PNAS*, **112**, 12249
- Weinmann, S. M., Pasquali, A., Oppenheimer, B. D., et al. 2012, *MNRAS*, **426**, 2797
- Weisz, D. R., Dolphin, A. E., Skillman, E. D., et al. 2014, *ApJ*, **789**, 147
- Weisz, D. R., Dalcanton, J. J., Williams, B. F., et al. 2011, *ApJ*, **739**, 5
- Williams, G. Grant, Olszewski, Ed, Lesser, Michael P., & Burge, James H. 2004, *Proc. SPIE*, **5492**, 787
- Wylezalek, D., Zakamska, N. L., Greene, J. E., et al. 2018, *MNRAS*, **474**, 1499
- Yan, R., Tremonti, C., Bershady, M. A., et al. 2016, *AJ*, **151**, 8
- Yan, R., Chen, Y., Lazarz, D., et al. 2019, *ApJ*, **883**, 175
- Yang, X., Mo, H. J., van den Bosch, F. C., et al. 2007, *ApJ*, **671**, 153
- Young, T., Jerjen, H., López-Sánchez, Á. R., & Koribalski, B. S. 2014, *MNRAS*, **444**, 3052
- Zahid, H. J., Kudritzki, R.-P., Conroy, C., Andrews, B., & Ho, I. T. 2017, *ApJ*, **847**, 18
- Zhou, S., Mo, H. J., Li, C., Boquien, M., & Rossi, G. 2020, *MNRAS*, **497**, 4753